

Department of Precision and Microsystems Engineering

Imaging the SAW Field on Suspended 2D Membrane

Yue Sun

Report no : 2023.063
Coach : Dr. Gerard Verbiest, Dr. Sabina Caneva
Professor : Dr. Gerard Verbiest, Dr. Sabina Caneva
Specialisation : DMN
Type of report : MSc Thesis
Date : 22 August 2023

Imaging the SAW Field on Suspended 2D Membrane

by

YUE SUN

Student Name	Student Number
YUE SUN	5503000

Supervisor:
Dr.Sabina Caneva
Dr.Gerard Verbiest
Faculty:
Faculty of 3ME, Delft

Abstract

Surface acoustic wave (SAW) is widely used in biological research and sensor applications, a comprehensive understanding of SAW propagation and visualization on suspended 2D membranes is crucial for the manipulation of nanoparticles in biological research and sensitivity improvement of SAW sensors based on 2D material. The initial step of this project involved exciting a standing SAW field on the SAW device and attempting to use Digital Holography Microscopy (DHM) for imaging the standing SAW field on the substrate. This attempt was very challenging and unfortunately was not successful. We used an Atomic Force Microscope (AFM) as an alternative solution for SAW field imaging. Initially, AFM was used to image the SAW field on the SAW device substrate, and the impacts of input frequency and power on the amplitude of the SAW field were investigated. Subsequently, microcavities were fabricated on the SAW device to record images of the SAW field within the microcavities and their surrounding areas, aiming to investigate the impact of microcavities on the SAW field. Finally, the prepared graphene membrane was transferred to the microcavities, the SAW propagation was recorded on the suspended membrane and the influence of the suspended membrane on SAW propagation was analyzed.

acknowledgments

I would like to express my heartfelt gratitude to Sabina and Gerard, for their invaluable guidance and continuous support throughout the research process. They gave me a lot of valuable feedback at the weekly group meeting, which helped my project towards a hopeful direction as we set before. I am also thankful to Hande and Yu Ze, whose thoughtful discussions of AFM application and SAW field characterization greatly enriched the content of this paper. Additionally, I want to thank friends and family for their unwavering encouragement and understanding during the 2-year study at TU Delft. Finally, I would like to acknowledge the countless researchers whose foundational work paved the way for this study.

Contents

Abstract	i
acknowledgments	ii
1 Introduction	1
2 Theoretical Fundamental	4
2.1 SAW Device	4
2.1.1 Introduction of SAW	4
2.1.2 Introduction of SAW Device	4
2.1.3 Fabrication of SAW device	6
2.2 Digital Holography Microscopy(DHM)	6
2.2.1 Introduction of DHM	6
2.2.2 Spatial resolution of DHM	7
2.2.3 Maximum Amplitude Resolved by DHM	8
2.3 AFM	8
2.3.1 AFM Working Principle and Different Mode	8
2.3.2 Ultrasonic Force Microscopy	10
2.3.3 SAW-AFM	10
2.4 2D Materials and 2D Materials Transfer	12
2.4.1 Fabrication methods of 2D material	12
2.4.2 Transfer Method of 2D Material	13
3 SAW Device Characterization	15
3.1 Simulation of SAW Device	15
3.2 S21 Parameter Characterization	18
4 Suspended membrane	21
4.1 Microcavities	21
4.1.1 Fabrication Methods	21
4.1.2 Characterization Methods	21
4.1.3 Fabrication Parameters	22
4.2 Graphene Membranes	24
4.2.1 Thickness characterization	24
4.2.2 Suspended Membrane Characterization	26
5 Direct Imaging	29
5.1 Methods to increase the measured frequency of DHM	29
5.1.1 Stroboscopic Effect	29
5.1.2 Amplitude Modulation	31
5.2 Measurement With DHM	34
5.3 Failure Reason	37
6 AFM Imaging	39
6.1 Setup of the SAW Field Imaging	39
6.2 Imaging the SAW field on the SAW device substrate	40

6.3	Imaging the SAW field on the substrate with microcavities	41
6.4	Imaging the SAW field on the suspended membrane	43
6.4.1	SAW Field on Suspended Graphene Membrane	43
6.4.2	SAW Field on Graphene Membrane and <i>LiNbO₃</i> Substrate	45
7	Conclusion and Outlook	49
	References	51

1

Introduction

Since Lord Rayleigh first discovered surface acoustic wave(SAW) and predicted its propagation properties in 1885[1], people started to apply the SAW in geophysics. In 1965, White and Voltmer invented interdigital transducer(IDT) which expands the application of SAW to electronic components. At present, SAW technology has been widely used in biomolecule control, mobile communication, sensor design and many other fields.

In the field of biological research, acoustic force is a good mode of force application in the characterization of some protein molecules and manipulation of nanoparticles. Coste et al. reported 2 kinds of proteins Piezo1 and Piezo2 which are required for mechanically stimulated cation conductance in cells[2] and provided compelling evidence shows that Piezo proteins are indeed ion channels[3]. After discovering that Piezo proteins are indeed ion channels, people began to construct biological platforms to study the effects of various factors on Piezo proteins. SAW has been widely used to study molecules on biological membranes due to its property of only propagating along surfaces and acting on a single protein molecule. In biological science and engineering, many kinds of chemical, optical, and electrical approaches have been developed to enable biomolecule detection. However, chemically functionalized surface patterning often requires predefined templates to transfer patterns through multi-step lithography[4]. Optical tweezers, though exhibiting very high force and spatial resolutions, rely on particle optical properties and could be compromised by laser damage of biological samples[5]. Dielectrophoresis, depending on the particle polarizability and medium conductivity, could also cause adverse physiological effects through electrical current-induced heating and electric field interactions[6]. Due to the relatively low power requirements and superior biocompatibility of SAW technology, SAW actuators are considered to have great potential in the field of nanoparticles and biomolecular manipulation. Jia et al. developed a micromechanical resonating membrane platform to manipulate and pattern nanoparticles and successfully manipulated multiple particles into various patterns of particle clusters[7]. Imaging SAW propagated on 2D membranes can help us control protein channels, nanoparticles and biomolecular better and it can be the first step to build a biological platform to study the protein channel. In the field of sensors, the SAW sensor has a wide range of applications in measuring gas, temperature, pressure, weight and more. The first generation of SAW gas sensors was developed decades ago, after decades of development, current SAW gas sensors can detect gas with high precision. Schedin et al. reported the detection of single gas molecules adsorbed on graphene, showing the application prospect of graphene membrane in ultra-high precision gas detection[8]. Such high sensitivity is attributed to: i) graphene has large specific surface areas ($2630 \text{ m}^2 \text{ g}^{-1}$). Every atom of graphene can be considered as a surface atom, capable of interacting even with a single molecule of the target gas or vapour species, which even-

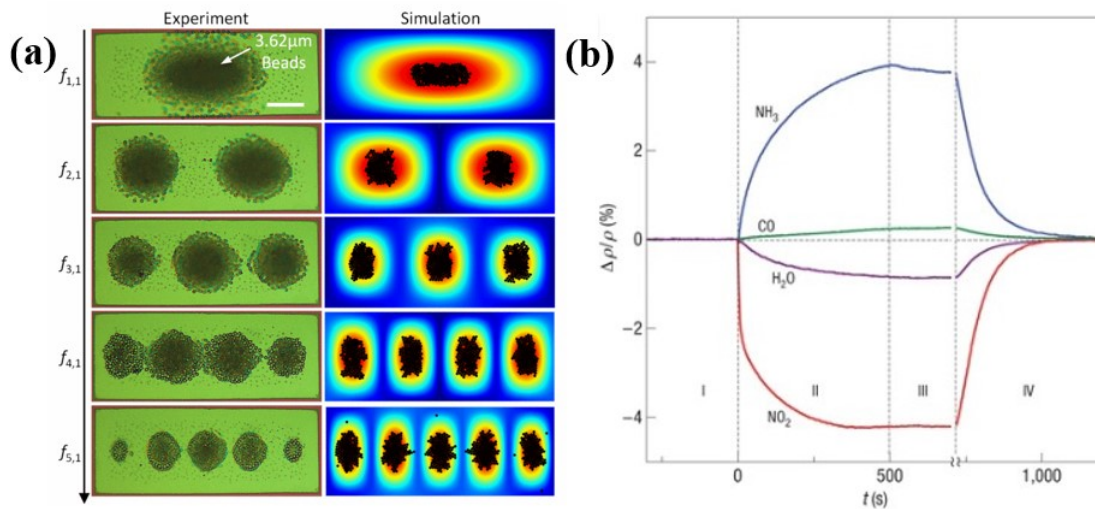


Figure 1.1: (a) Chladni patterning of microparticles in water by using a rectangular membrane. A group of $3.6\mu\text{m}$ SiO_2 microbeads are manipulated into diverse cluster patterns[7]. (b) Changes in resistivity, ρ , at zero B caused by graphene's exposure to various gases diluted in concentration to 1 p.p.m. The positive (negative) sign of changes is chosen here to indicate electron (hole) doping. Region I: the device is in the vacuum before its exposure; II: exposure to a 5l volume of a diluted chemical; III: evacuation of the experimental set-up; and IV: annealing at 150°C . The response time was limited by our gas-handling system and a several-second delay in our lock-in-based measurements[8].

tually results in the ultrasensitive sensor response [9]. ii) The interaction between graphene sheets and adsorbates could vary from weak van der Waals interactions to strong covalent bonding. All of these interactions will perturb the electronic system of graphene, which can be readily monitored by convenient electronic methods[10]. In the SAW chemical sensor, a functionalized layer is covered on the SAW substrate and the frequency of SAW will change when functionalized layer absorbs the chemical targets, SAW chemical sensor can obtain relevant information about the detected object with the frequency shift. The sensing layer is a critical component of sensor design, and a wide variety of sensing layer materials have been explored for both chemical and biological SAW sensors, graphene oxide, which has a large surface area to volume ratio along with hydrophilic functional groups, has been used for humidity sensing applications[11]. Imaging SAW on a suspended membrane can help us know how SAW propagates on a suspended membrane which can help us improve the sensitivity of SAW sensors based on 2D material.

In the field of mobile communication, SAW devices can be used to make filters, which are widely used in RF front-end modules of various electronic devices. In the 5G era, the SAW market scale is very considerable. Due to the requirements of low power consumption and small size, smartphones currently use small-volume and high-performance acoustic filters, including surface acoustic wave (SAW) filters and bulk acoustic wave (BAW) filters, which have different characteristics and application frequency bands. For the SAW filter, a very effective way to reduce its power consumption and improve sensitivity is to fabricate some microcavities on the saw propagation substrate and fill microcavities with waveguide materials[12]. Imaging the SAW propagated on the surface with microcavities is the first step to studying how will SAW propagates on the surface with microcavities filled with waveguide material.

In the above fields, whether we are studying cell membranes, filters or designing new-generation sensors, we will all involve the imaging of SAW on multilayer membranes. Nowa-

days, the measurement of SAW propagated on a 2D membrane mainly focuses on characterizing the waveform, frequency and wavelength, while the progress in imaging of SAW field on a 2D membrane is slow. On the official website of Lync'ee Tec[6], we can find the images of the SAW field (frequency at 24.7 MHz) imaging with DHM. It has been proven to be a feasible method to image the SAW field with DHM, however, SAW propagated on 2D membranes imaging using DHM still needs to be explored. The realization of direct imaging of the SAW field on a 2D membrane helps us to study the characteristics of SAW propagation on the 2D membrane.

In this project, we focus on imaging the SAW field in different kinds of propagation surfaces and finding how SAW propagation affects by membrane parameters. We used COMSOL to simulate the SAW field on the different substrates and imaged the SAW amplitude using atomic force microscopy (AFM).

In this thesis, we answer the following questions:

- How do we image the SAW field?
- What is the difference between the propagation of the SAW in microcavities and substrates when SAW propagates on the surface with microcavities?
- Is the propagation of SAW on the suspended 2D membrane the same as that on the surface, and how does the 2D membrane affect the propagation of the SAW?

In this project, we will develop an imaging method to image the SAW field propagated on a 2D membrane. We focus on using the optical method to image the SAW field in different kinds of propagation surfaces and finding how does SAW propagation affect by membrane parameters. This report starts with the background information about the SAW field, 2D membrane, imaging methods and the preliminary design of the project in Chapter 2. In Chapter 3, we introduce the simulation work and the measurement of the S parameters of the SAW device. After that, we introduce the fabrication of the suspended membrane and the measurement method of the graphene thickness in Chapter 4. In Chapter 5, we use DHM to image the SAW field and analyse the reason why we can not image the SAW field by using DHM. In Chapter 6, we discuss the measured SAW field in a suspended membrane and analyse the factor which affects the SAW propagated on the microcavities and suspended membrane. In Chapter 7, we review the entire project process and make prospects for future work.

2

Theoretical Fundamental

2.1. SAW Device

2.1.1. Introduction of SAW

In 1885, Lord Rayleigh first discovered SAW and predicted its propagation properties[1], Rayleigh wave is also named after him. Rayleigh wave is a kind of SAW which propagate along the solid surface, it contains longitudinal and transverse motions. The increase of the distance from the surface leads to a decrease in Rayleigh wave amplitude, there are phase differences between these constituent motions. In homogeneous and isotropic solids, the Rayleigh wave cause the motion of surface particles in an ellipse in a plane perpendicular to the surface and parallel to the propagation direction, the long axis of the ellipse is vertical to the surface. When the Rayleigh wave travels along the surface from left to right, the in-plane motion of a particle is counterclockwise, as shown in Figure 2.1(a). In addition, Lord Rayleigh showed that as the depth of the material increases, the motion amplitude attenuation and eccentricity change and the velocity of the surface wave is smaller than that of the body wave. Rahman and Barber found that the velocity of the surface is the root of the equation shown as follows[13]:

$$R(V) = (2 - M_2^2)^2 - 4\sqrt{(1 - M_1^2)(1 - M_2^2)} \quad (2.1)$$

M_1 and M_2 are $\frac{V}{c_1}$ and $\frac{V}{c_2}$ respectively, where $c_1 = \sqrt{\frac{\lambda + 2\mu}{\rho}}$ is dilatational wave speeds and $c_2 = \sqrt{\frac{\mu}{\rho}}$ is shear wave speeds, λ and μ are the Lamé constants of the used material.

It is clear that there is only 1 real root when $v_R \in (0 - c_2)$ and the form of the root is very complex, so it is important to find the simplified expression for the root of equation 2.1 in many elastodynamic boundary value problems, the simplified expression for the root will be mentioned in the next section.

2.1.2. Introduction of SAW Device

In 1965, White and Voltmer invented the interdigital transducer(IDT) which plays a decisive role in SAW device[15]. IDT is a device that consists of two interlocking comb-shaped arrays of metallic electrodes, as shown in Figure 2.1(b), these electrodes are applied on a substrate made of piezoelectric material such as Quartz or $LiNbO_3$. IDTs generate a periodic electric field by applying an alternating voltage to the two arrays of electrodes, there will be alternating regions of tension and compression at the surface due to the piezoelectric substrate. The standing SAW field is generated as a result of the periodic strain field on the substrate, thus converting electrical energy into mechanical energy to generate SAW. IDTs can also complete

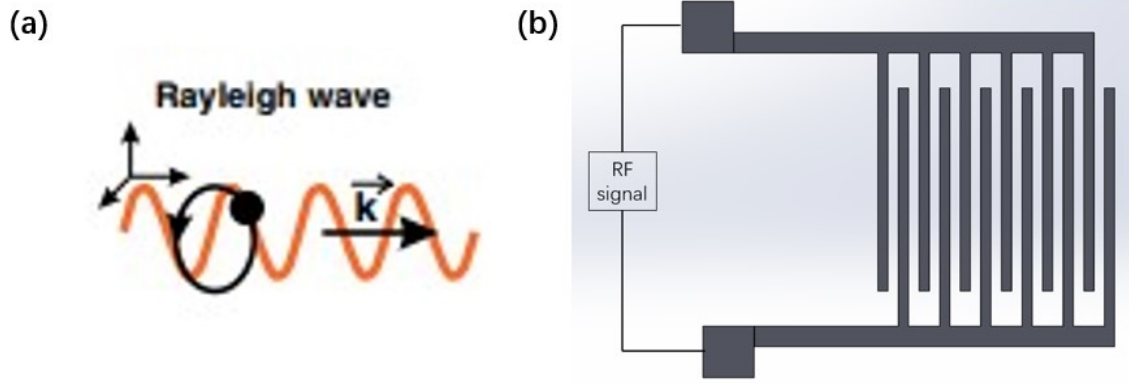


Figure 2.1: (a) Particle Motion of Rayleigh Wave[14]. (b) Sketch diagram of IDT

the conversion of mechanical energy to electrical energy, when SAW are transmitted to IDTs, IDTs can also convert SAW into electrical signals.

Since the main energy of SAW is concentrated on the surface, when there are some slight changes on the transmission surface, the transmission of SAW will be affected by the surface change, therefore, the SAW device can be used as a high-sensitivity sensor. Many factors affect the surface state, including pressure, temperature, humidity and so on. Therefore, SAW devices can be used as temperature, pressure, humidity, and other sensors that realize detection based on changes in surface state.

Usually, the SAW sensor works based on changes in eigenfrequency or velocity caused by changes in the external environment. Compared to the velocity of SAW, the change in eigenfrequency is easier to detect and there is currently no accurate expression for the velocity of SAW in the material. The velocity of the SAW in different materials and under different conditions can only be measured and cannot be calculated, so sensors based on SAW velocity changes are still in a state waiting for development. Due to the application significance of the Rayleigh wave velocity, a simple and approximate expression for analyzing SAW speed is necessary. Many equations for SAW velocity had been developed in papers, one of the most famous approximate equations for the isotropic material is shown as follow[16]:

$$v_R = v_t * \frac{0.87 + 1.12\nu}{1 + \nu}, \nu \in [0 - 0.5] \quad (2.2)$$

where $v_t = \sqrt{E/2\rho(1 + \nu)}$, ρ is the material density, E denotes the Young's modulus and ν is the Poisson's ratio. Based on Equation 2.2, we can calculate the eigenfrequency of the SAW device using formula $f = \frac{v_R}{\lambda}$

When a radio frequency (RF) signal is applied to the electrodes, a travelling SAW will be on the SAW device surface due to the piezoelectric effect. To observe the SAW field, we decided to activate a standing SAW field on the surface of the SAW device. As shown in Figure 2.1(c), applying an excitation signal $u = A * \cos(\omega t - kx + \frac{\pi}{2})$ to the IDT electrodes on one side, a travelling SAW will propagate along the direction of electrode arrangement on the surface. After the SAW reach another side of the IDT electrodes, the SAW will be reflected, the wave equation of SAW and reflected SAW can be expressed as:

$$u_1 = A * \cos(\omega t - kx + \frac{\pi}{2}) \quad (2.3)$$

$$u_2 = A * \cos(\omega t + kx + \frac{\pi}{2}) \quad (2.4)$$

These two waves are superimposed and a standing SAW field is generated, and the wave equation of standing SAW is given:

$$u = u_1 + u_2 = A * \cos(\omega t - kx + \frac{\pi}{2}) + A * \cos(\omega t + kx + \frac{\pi}{2}) = A * \cos kx * \cos \omega t \quad (2.5)$$

To make the SAW strongest, the frequency of the RF signal applied on the SAW device should be equal to the eigenfrequency of the IDT transducer ω_0 . Moreover, the IDT width a , IDT spacing b and frequency satisfy the following

$$a = b = \frac{\lambda}{4} = \frac{v_s}{4f} \quad (2.6)$$

2.1.3. Fabrication of SAW device

The fabrication of the SAW device is shown in Figure 2.2. Initially, clean the $LiNbO_3$ substrate, coat a photoresist(PR) layer on the substrates then expose thoroughly without a mask. Then another PR layer is coated onto this exposed PR to form a thick PR layer, there will be a mutual dissolution between two PRs. After the photoresist patterning, the substrates were placed into the magnetron sputtering chamber to for metal layer deposition. After sputtering, the substrates are soaked in acetone aided by ultrasonic vibration to remove the PR to form the IDT patterns in the SAW.x

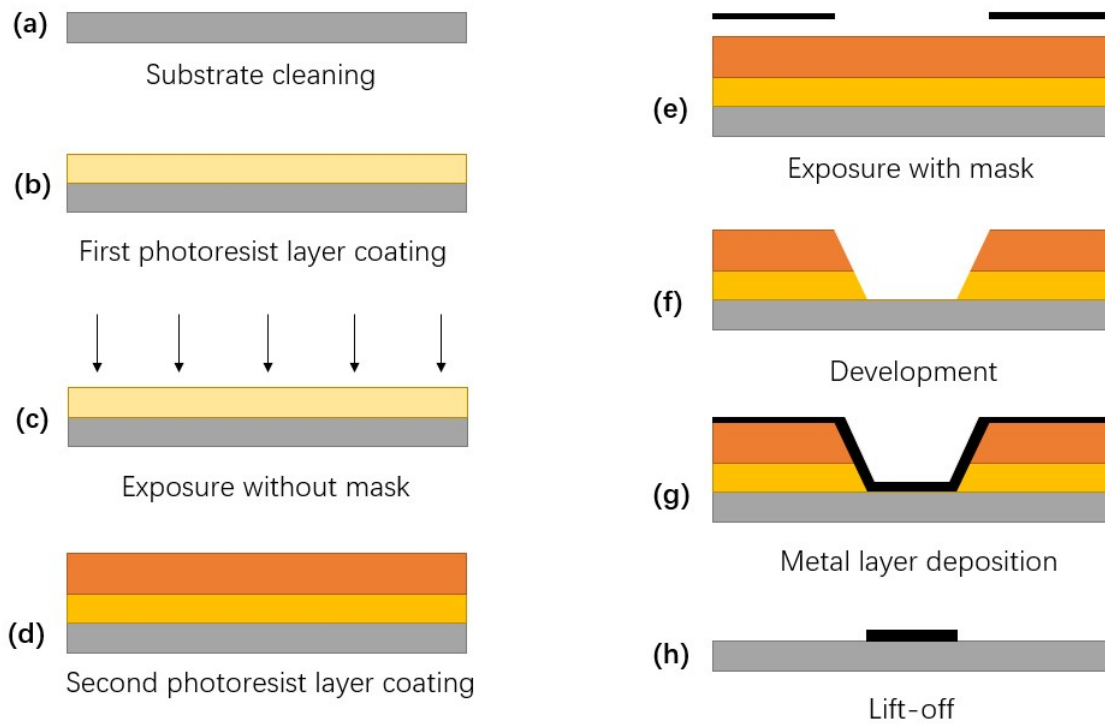


Figure 2.2: Schematic diagrams of SAW device fabrication

2.2. Digital Holography Microscopy(DHM)

2.2.1. Introduction of DHM

Digital holography is a very effective method to achieve high-precision measurement for a micron scale surface. Compare with other microscopy methods which rely on recorded objects by projected image, DHM digitally records the wavefront information from the object into a

hologram and then reconstructs the image of the object from the hologram by using a computer reconstruction algorithm[17]. The working principle of DHM is shown in Figure 2.3, a laser beam generated by a laser source divided into two laser beams after transmission of the beam splitter, one of them illuminates the specimen and diffracts, and then the diffraction wave sent to the image sensor, this wave is called as objective wave. Another laser beam called as reference wave is directly received by the image sensor, and the interference image of these two waves is recorded by the image sensor and sent to the computer to reconstruct the surface image[18]. There are two configurations of DHM: off-axis DHM and phase-shifting DHM. Off-axis DHM can only record a single hologram due to the different propagation directions of two waves while phase-shifting DHM can record multiple in-line holograms by changing the phase of reference wave[19].

The DHM system usually consists of an illumination source, interferometer, digitizing camera and computer with the necessary program, laser source is usually used as an illumination source due to the high coherence of the laser. There are two kinds of interferometer used in the DHM system, the Michelson interferometer and the Mach-Zehnder interferometer, when the objective wave is reflected from the specimen, the Michelson interferometer will be used, Mach-Zehnder interferometer will be used when the objective wave transmits the specimen[18].

Brunn et al. used the DHM manufactured by Lyncee tec company to achieve the measurement of the rough surface in sub-micrometre accuracy[20]. Singh et al. reported a method used to image the SAW field on soft materials, this method uses a temporal phase-shifting algorithm to reconstruct the phase image of the SAW field and it can be widely used in characterizing the biomechanical properties of the tissues [21].

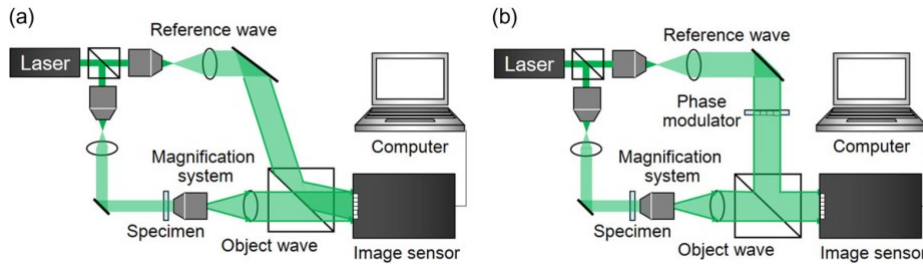


Figure 2.3: Schematic diagrams of (a) off-axis and (b) in-line digital holography systems[18]

2.2.2. Spatial resolution of DHM

For microscopes, the spatial resolution determines the minimum size they can distinguish. When two infinitesimal objects in the sample observed by the microscope are Rayleigh distance apart (Rayleigh distance is $\frac{0.61\lambda}{NA}$ where NA is the numerical aperture and λ is the wavelength of light illumination), two airy disks will be formed in the imaging system, as shown in Fig 2.4. Since DHM uses a laser(a kind of coherent light) as the illumination source, the intensity of the image is equal to $|O_1 + O_2|^2$. When the phases of $|O_1|$ and $|O_2|$ are the same, these two patterns cannot be resolved. When the phases of $|O_1|$ and $|O_2|$ are opposite, the pattern of both can be well resolved, which is also the minimum distance that the system can resolve. To sum up, there is no simple formula to describe the resolution of DHM, Gao et al. reported a formula that can describe the resolution of DHM[22]. Factor k_1 is determined by the experimental parameters, such as the coherent noise level and the SNR of the detector, etc.

$$\sigma = \frac{k_1 \lambda}{NA} = \frac{k_1 \lambda}{NA_{imag} + NA_{illum}} \quad (2.7)$$

From this formula, we can see that there are two factors related to the resolution of DHM, the first is the wavelength of the laser, and the second is the NA of the illumination system and imaging system. Since the laser source of DHM is immutable which means that the wavelength of the laser can not be changed, we will reduce the NA of the imaging system as much as possible.

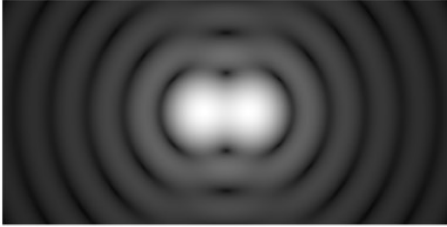


Figure 2.4: The distance to the first minimum (the Rayleigh criterion)

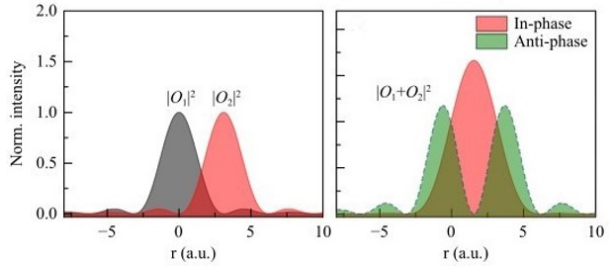


Figure 2.5: Intensity distribution of the Airy disks[22]

2.2.3. Maximum Amplitude Resolved by DHM

Due to the limitation of laser wavelength, the phase image of the object has a wrapped phase in $[-\pi, \pi]$. When the height difference of the surface is more than half the wavelength of the laser, the reconstruction algorithm will have errors. Qin et al used 532nm wavelength light as the illumination source to characterize a spherical surface with a height difference of $5\mu m$ and obtained Figure 2.6. From this figure, we can see that because the height difference is much greater than a wavelength, the phase configuration we get is a ring with phases ranging from $-\pi$ to π .

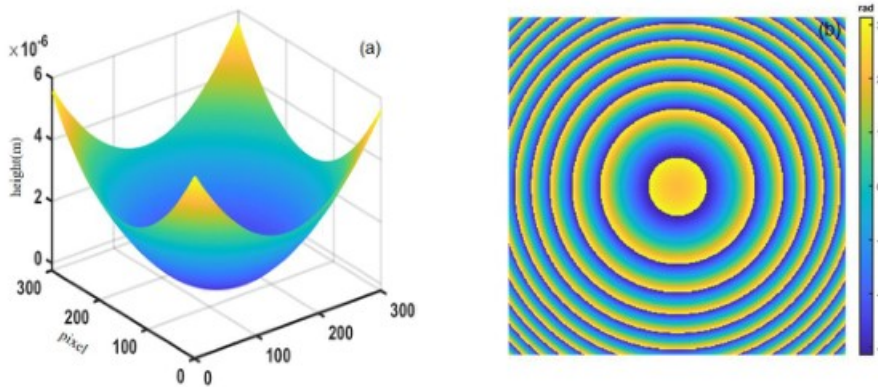


Figure 2.6: A spherical surface and its wrapped phase maps at 532 nm[23]

2.3. AFM

2.3.1. AFM Working Principle and Different Mode

Atomic Force Microscope (AFM) is a microscope that uses a micro-cantilever to detect the force between the tip apex and the surface with atomic-level resolution. An AFM system is usually composed of a micro-cantilever with a tip, a micro-cantilever motion detection device, a feedback loop for monitoring the motion of the tip of the micro-cantilever, a piezoelectric ceramic scanning device for scanning the specimen, and a computer system which used for image acquisition, display, and processing.

The working principle of AFM that: fix one end of the probe which is sensitive to weak force, and there is a tip which lightly contacts the sample surface on the other end. As shown in Figure 2.7, the laser beam emitted by the Laser Diode is focused on the back of the cantilever and is reflected from the back of the cantilever to a laser spot position detector composed of photodiodes. During sample scanning, due to the interaction force between the atoms on the sample surface and the atoms at the tip apex of the probe, the probe will bend with the surface topography of the sample, and the reflected beam will also shift accordingly. Therefore, by detecting the changes in the position of the light spot through a photodiode, information on the surface topography of the tested sample will be obtained.

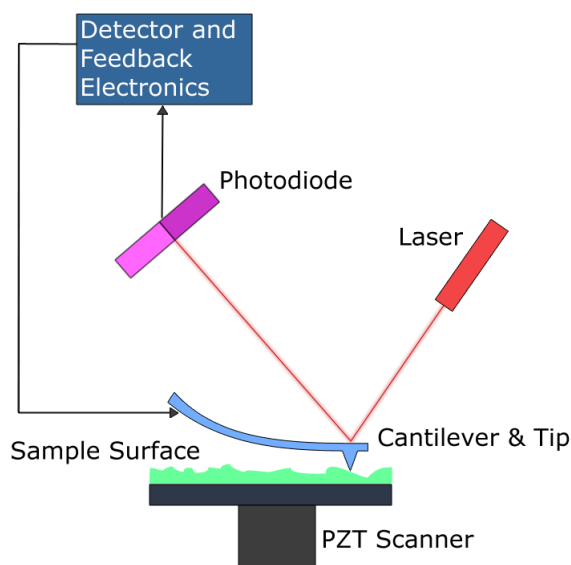


Figure 2.7: Schematic diagram of AFM

The working mode of the AFM is classified in the form of the force between the tip and the sample, when AFM is used to map the field, it has 3 image modes: contact mode, tapping mode and non-contact mode.

Contact Mode In contact mode, the tip is to contact the measured surface directly, the force between the tip apex and the surface will deflect the cantilever, and the surface image will be built based on the cantilever deflection. During scanning, the force exerted by the cantilever on the tip may damage the surface structure of the sample, so if the surface of the sample is soft and cannot withstand such force, it is not suitable to choose the contact mode for imaging the sample surface.

Non-contact Mode When detecting the surface of the sample in non-contact mode, the cantilever oscillates at a distance of $5 - 10nm$ above the sample surface. The interaction between the sample and the needle tip is controlled by van der Waals forces, usually $10^{-12}N$. The sample will not be damaged and the probe tip is not contaminated, making it particularly suitable for studying the surface of soft objects. The disadvantage of this operating mode is that achieving it in a room-temperature atmospheric environment is very difficult. Because a thin layer of water will inevitably accumulate on the surface of the sample, it will build a small

capillary bridge between the sample and the needle tip, sucking the probe tip and the surface together, thereby increasing the pressure on the surface from the tip.

Tapping Mode In tapping mode, the cantilever oscillates above the sample surface at its resonant frequency, and the needle tip only briefly strikes the sample surface periodically. This means that the lateral force generated when the tip contacts the sample is significantly reduced. Therefore, when detecting soft samples, tapping mode is one of the best choices.

2.3.2. Ultrasonic Force Microscopy

Ultrasonic Force Microscopy(UFM) is a kind of microscopy which detects the ultrasonic vibration on the surface based on the nonlinearity of the tip-surface interaction. The schematic of the tip-surface interaction is shown in Figure 2.8(a). when the cantilever contacts a non-vibrating sample at h_1 , there will be a repulsive force $F(h_1)$ exerted on the cantilever. When there is vibration on the sample at a high frequency such as the surface with the standing SAW field, the cantilever will not follow the surface vibration due to the vibration frequency is much higher than the resonance frequency of the cantilever. When measuring the high-frequency vibration, the cantilever will respond to the force averaged in time during one ultrasonic period. For small deflections such as a_0 , the averaged force is equal to the initial force $F(h_1)$. For high deflections such as a_1 or higher, the contact between the cantilever and the surface will be broken in part of the ultrasonic period and the averaged force will be increased sharply when the amplitude is a_1 , as shown in Figure 2.8(b).

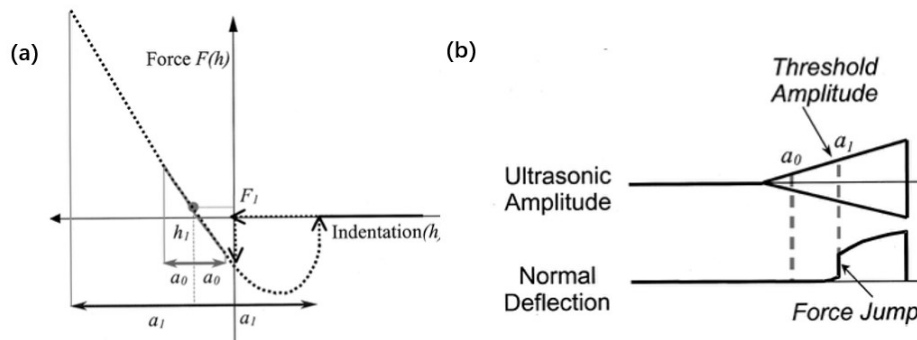


Figure 2.8: (a)Schematic of tip-surface interaction curve. (b)Schematic of increasing ultrasonic amplitude inducing an amplified cantilever deflection.[24]

2.3.3. SAW-AFM

SAW is a kind of acoustic wave with a high frequency which is much higher than the resonance frequency of the AFM cantilever, to detect the SAW propagation along the surface, we need to find a method to detect a high-frequency signal in the nanoscale. Scanning acoustic force microscopy(SAFM) is an ultrasonic scanning probe microscopy which detects waves that have interacted with the elastic system, and allows for the detailed mapping of SAW amplitudes within SAW devices. In 1997, T. Hesjedal et al. first reported the visualization of the SAW field within an IDT by SAFM with submicron lateral resolution and discussed how the mass loading in different layer thicknesses affects the oscillation amplitude pattern [25]. In 2001, D. R. Oliver et al. developed a method which can obtain the stroboscopic image of the SAW field by using a heterodyne electrostatic force scanning probe microscopy and imaged the SAW field with a frequency of 434 MHz [26]. In 2011, Fanghao Li et al. reported an AFM-based probe heterodyne system for SAW detection, used it to detect laser-induced SAW and the measured amplitude reached 30 nm [27].In 2022, Hellemann et al. reported a method to

measure the amplitude of the standing SAW via AFM, in the experiment, they found that the energy transfer between the vibrating surface and the cantilever will lead to the deflection exceeding the surface modulation[28]. To eliminate this error, they developed a method based on comparing force-curve measurements with the equation of motion of a driven cantilever and demonstrated the image of the SAW field with a resonance frequency near $3GHz$ on GaAs substrate.

The working principle of the SAFM for the SAW field amplitude image is shown as Figure 2.9. An RF signal generator is used to generate the RF signal used to excite the SAW device, the generated signal will be amplitude modulated by the LF signal. The LF signal is set as the reference signal of the lock-in amplifier which means that the output of the lock-in amplifier will be the amplitude information of the SAW field, the output of the lock-in amplifier will be sent to AFM's digital signal processing (DSP) board and computer to image the SAW field.

Lock-in amplifier is an amplifier which can extract signals with known carriers that are buried

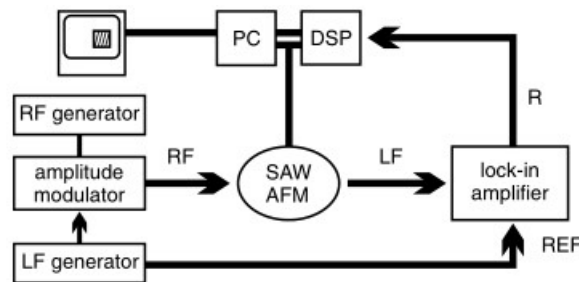


Figure 2.9: Schematic of amplitude mode SAFM[14]

in noise. It is essentially a homodyne detector followed by a low-pass filter, which can usually adjust the cutoff frequency and filter order. For a lock-in amplifier, there are 2 inputs, a repetitive signal to be measured and a reference signal which is the same frequency and has a fixed phase relationship to the signal buried in the noise. The output of the lock-in amplifier is a single value which represents the amplitude of the sine wave and the phase relationship between the signal and the reference.

Based on the methods and explanations mentioned before, we developed a method to image the SAW field, as shown in Figure 2.10. In this method, we use an RF generator to generate the RF signal which has the same frequency as the eigenfrequency of the SAW device and use a LF generator to generate the LF signal, the LF signal has two purposes: one is for amplitude modulation processing with the generated RF signal, and the other is used as a reference signal for lock-in amplifier. The modulated RF signal will be the excitation signal of the SAW device and the generated SAW field will cause the deflection of the cantilever and it will be measured with optical lever technology, where the beam emitted by the laser diode is reflected from the cantilever and detected by the quadrant photodiode. The cantilever deflection caused by the SAW field will be amplitude modulated and the deflection information will be sent to the lock-in amplifier. After being processed by the Lock-in amplifier, the cantilever deflection caused by SAW will be sent to the software and as the result of the SAW field scan.

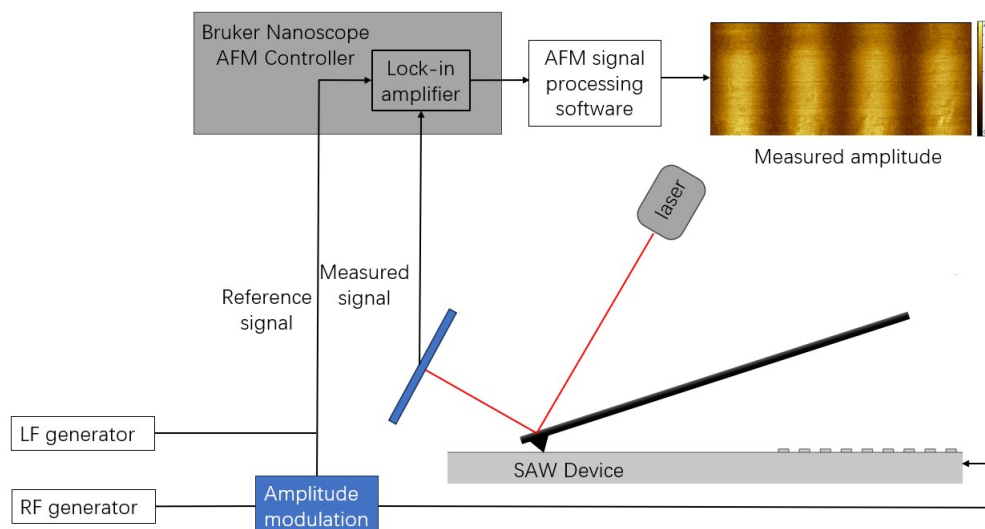


Figure 2.10: Schematic of the SAW field image method.

2.4. 2D Materials and 2D Materials Transfer

The research on 2D materials can be traced back to the single-layer graphene obtained by mechanical exfoliation from bulk graphene, and many 2D materials have been found at that time, such as hexagonal-Boron nitride(h-BN), Black phosphorous(BP), Molybdenum disulfide (MoS_2) and so on. In our project, we focus on the propagation of SAW on suspended 2D material, so the focus on 2D materials is on those aspects related to the propagation of SAW on 2D material. In this section, we will introduce the fabrication methods of 2D material and how to transfer 2D material on microcavities.

2.4.1. Fabrication methods of 2D material

At present, there are two methods most widely used in the fabrication of 2D materials, mechanical peeling and chemical vapour deposition[29]. In this section, we will introduce these two methods and some new methods that are not so widely used.

Mechanical peeling When Novoselov et al. first separated graphene from graphite with scotch tape, they can only fabricate a small piece of graphene in micrometer-scale[30]. However, they can not control the thickness of the graphene flake which means that the place of monolayer graphene and the thickness of this flake is random. Although this method has some shortages, this small flake is big enough to find the unique properties of graphene.

Chemical Vapour Deposition(CVD) Although monolayer graphene was obtained for the first time with scotch tape, its fabrication efficiency is very low, people try to find a new method to produce monolayer graphene more effectively and get some larger monolayer graphene, CVD is the most effective method to produce monolayer graphene. Li et al. find a method to fabricate monolayer graphene, they copper substrate to grow graphene films, 95% of graphene films are monolayer graphene and graphene films are continuous on copper surface steps[31].

Other novel synthetic approaches Pulsed laser deposition(PLD), Glavin et al use 248 nm laser deposited ultra-thin h-BN film on pyrolytic graphite and sapphire substrates[32]. In pyrolysis of compounds containing B and N elements, Zhu et al. mixed different proportions of boric acid and urea in ultrapure water and dissolve them at high temperatures, they can

control crystal orientations by changing the crystal growth rate during the evaporation process and the ratio of boric acid and urea[33].

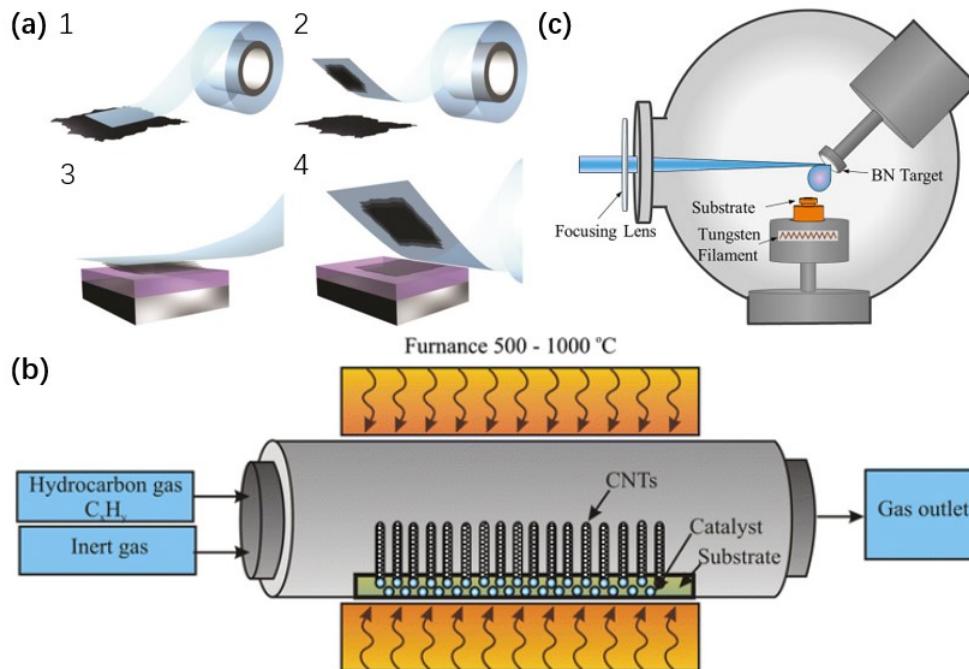


Figure 2.11: (a) Step by step of a mechanical exfoliation process: (1) adhesive tape is pressed against a HOPG surface so that the top few layers are attached to the tape (2), (3) the tape with crystals of layered material is pressed against a surface of choice, and (4) upon peeling off, the bottom layer is left on the substrate.[34]. (b) Schematic representation of chemical vapour deposition (CVD) process[35]. (c) Schematic of PLD setup[32].

In this project, the diameter of 2D material coated on microcavities is in tens of micrometres scale and the thickness varies from a few nanometers to ten nanometers. Considering that the 2D material size we need is small and the thickness requirement is low, mechanical peeling by scotch tape is the most appropriate method for this project.

2.4.2. Transfer Method of 2D Material

There are several transfer methods to place the 2D membrane in a different place, all-dry viscoelastic stamping, electrochemical process and some other transfer methods. In our project, we decide to use the all-dry viscoelastic stamping method to transfer 2D material and this subsection will only introduce this method.

The experimental set-up of this method contains optical microscopy, three axes micrometre stage and viscoelastic stamp, as shown in Figure 2.12(a). The stamp used in this method is a kind of viscoelastic material manufactured by Geipak, it is stuck on a glass slide to handle the sample conveniently.

This transfer method is based on viscoelasticity, the stamp behaves as an elastic solid in short action time while the stamp can flow in a long action time. When peeling off the stamp from the sample surface, there is a long action time which means the stamp will flow away slowly, the graphene flake will be released and adhere to the sample surface, as shown in Figure 2.12(b).

This transfer method can be applied to all kinds of 2D material which can be manufactured by mechanical exfoliation, in this project, when we need to study the influence of the material type of 2D membrane on SAW propagation, this method can help us transfer 2D membrane

manufactured by other material. Due to a lack of capillary force, this method can be used to fabricate suspended membranes, Castellanos et al. successfully transferred single-layer MoS_2 onto SiO_2 substrate with different sizes of microcavities to fabricate suspended membranes[36], as shown in Figure 2.12(c).

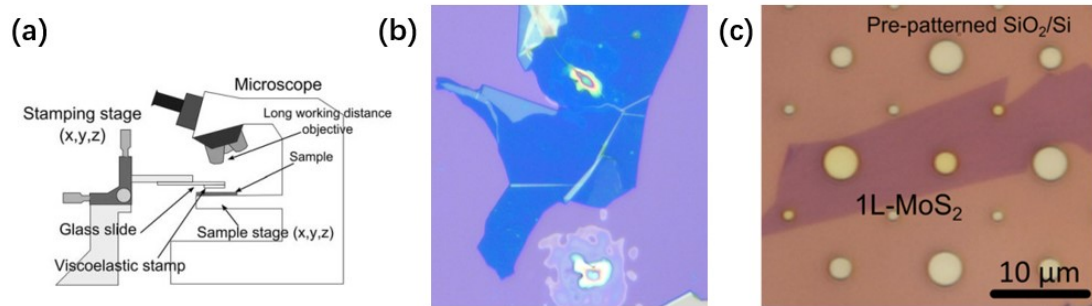


Figure 2.12: (a) Experimental set up of all-dry viscoelastic stamping[36]. (b) Microcavities covered with graphene membrane and without graphene membrane. (c) Single-layer MoS_2 on SiO_2 substrate with different sizes of microcavities[36].

3

SAW Device Characterization

3.1. Simulation of SAW Device

Before activating the SAW device and imaging the SAW field, we need to simulate the SAW device and SAW field. The parameters of the SAW device are shown in Table 3.1.

description	symbol	value
Thickness of 2D SAW device	h_{LN}	$500 \mu m$
Width of 2D SAW device	w_{LN}	$10 mm$
Number of electrode finger pairs	N_{fi}	32
Thickness of PML	T_{PML}	$50 \mu m$
Distance between IDTs	L_{tt}	$500 \mu m$
Electrode pitch	$Pitch_E$	$5 \mu m$
Finger pitch	$Pitch_F$	$10 \mu m$
Finger height	h_{fi}	$0.07 \mu m$
Finger width	w_{fi}	$2.5 \mu m$
Maximum meshsize	h_{max}	$2 \mu m$

Table 3.1: Parameters of Simulated SAW device.

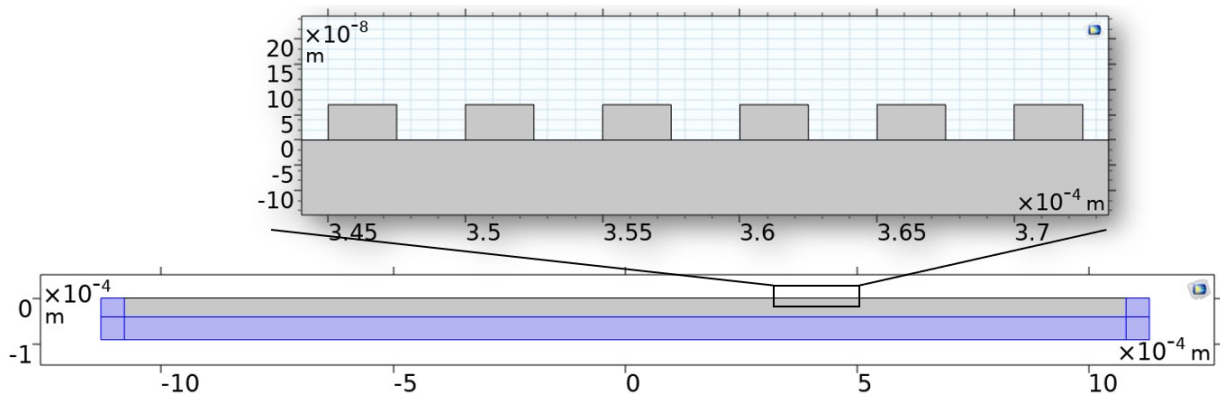


Figure 3.1: (a) Parameters of the measured SAW device. (b) Modal of the measured SAW device

In Figure 3.1, the blue part is the perfectly matched layer(PML) of the SAW device, the PML is a domain or layer that is added to an acoustic model to mimic an open and non-reflecting

infinite domain. In the frequency domain, the PML imposes a complex-valued coordinate transformation to the selected domain that effectively makes it absorb at a maintained wave impedance, thus eliminating reflections at the interface. In the time domain, additional equations are solved in the PML for the inverse Laplace transformed equations.

The SAW device is a two-port network; the two-port network is a device which has two pairs of terminals to connect to external circuits, the structure of the two-port network is shown in Figure 3.2. In this figure, a_1 and a_2 are incident waves, b_1 and b_2 are reflected waves, and

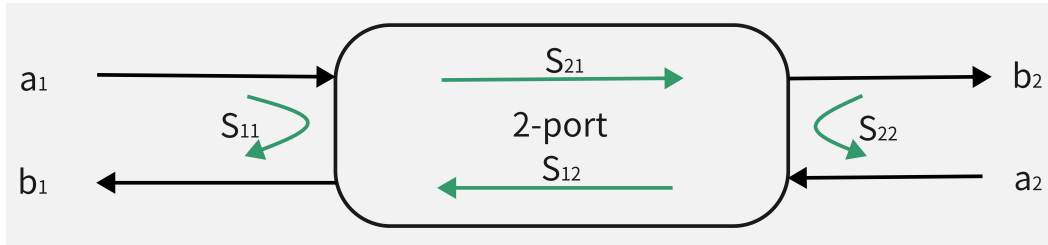


Figure 3.2: S parameter of two-port network

the scattering parameter(S parameter), which can be used to measure the reflection coefficient and transmission coefficient of electrical networks is measured in terms of incident and reflected waves at ports. S_{12} and S_{21} are transmission coefficient, S_{11} and S_{22} are reflection coefficient. The matrix description is shown as follow:

$$\begin{bmatrix} b_1 \\ b_2 \end{bmatrix} = \begin{bmatrix} S_{11} & S_{12} \\ S_{21} & S_{22} \end{bmatrix} \begin{bmatrix} a_1 \\ a_2 \end{bmatrix} \quad (3.1)$$

In the simulation part, we first do the simulation for S parameters which can be used to find the eigenfrequency of the SAW device, the simulated result of S_{21} is shown as Figure 3.3(a). We find that there are some peaks on the S_{21} curve and some valleys in the S_{11} curve. The peaks and the valley occurred around 362 MHz , and the eigenfrequency of the SAW device is 362 MHz . After we simulated the eigenfrequency of the SAW device, we conducted simulations on the SAW devices with microcavities on their substrates. Firstly, we simulated the effect of the depth of microcavities on the S_{21} parameter, and the result is shown in Figure 3.3(b). We executed a Frequency Domain study in two dimensions structure using the Solid Mechanics, Electrostatics and Multiphysics Piezoelectric Effect physics interfaces in COMSOL. By exploring the variation of S_{21} curve with frequency, we can explore the characteristic frequency and transmission efficiency of the SAW device. From Figure 3.3(b), we found that after preparing microcavities on the SAW device, the eigenfrequency of the SAW device will shift to the right by 0.5 MHz , the S_{21} parameter of the SAW device will almost not change with the change of depth of microcavities when the depth of the microcavities is relatively shallow ($< 0.5 \mu\text{m}$), so we do not strictly focus on the depth of the microcavities when fabricating them.

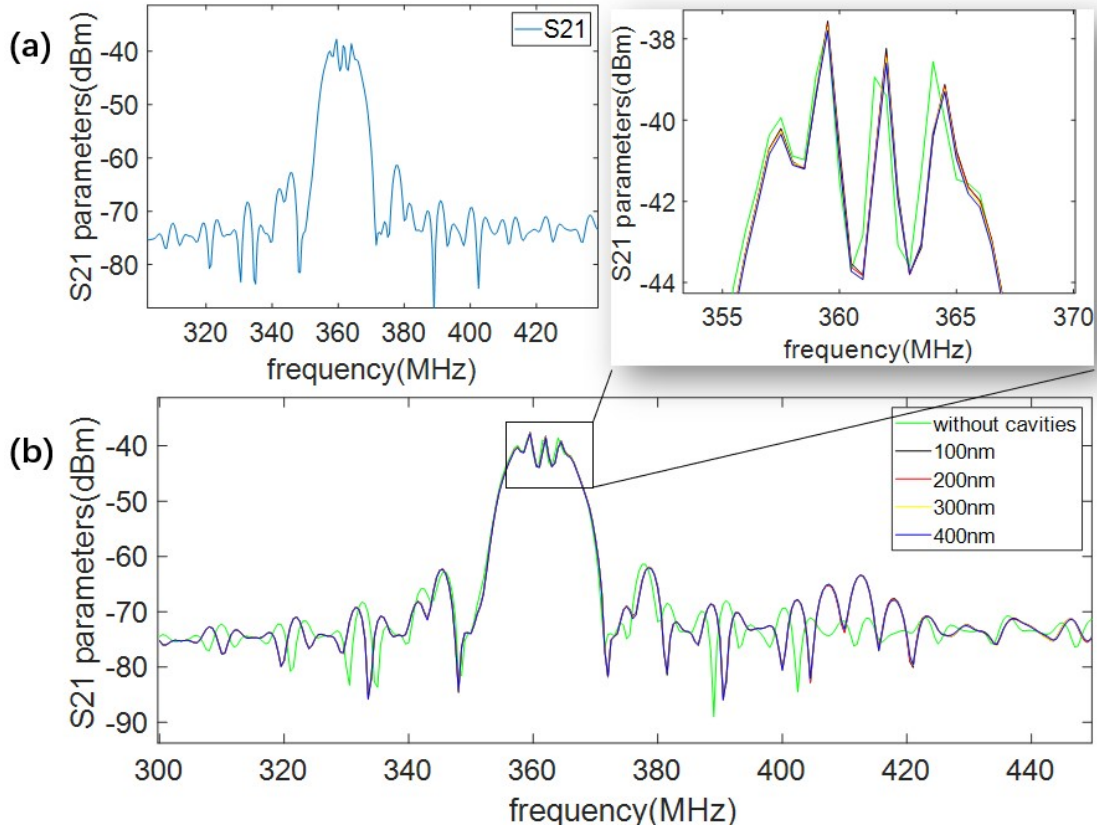


Figure 3.3: (a) Simulated S_{21} parameter of the SAW device. (b) Simulated S_{21} parameter of the SAW device with different depths of microcavities on the substrate.

Then, we simulated the effect of the width of microcavities on the S_{21} parameter, we fabricated microcavities on the modal of the 2D SAW device, the depth of the microcavities is $0.2 \mu m$ and the microcavities are located on the centre of the SAW propagated surface. The simulated result is shown in Figure 3.4, we found that the S_{21} curves with different widths of microcavities are basically the same, which means that the size of the width has no effect on the eigenfrequency of the SAW device. After that, we simulated the effect of the location of the microcavities on the S_{21} parameter. We simulated the S_{21} parameters of microcavities at a distance of IDTs from $25 \mu m$ to $425 \mu m$, with each distance change of $50 \mu m$, and plotted the curve of S_{21} with distance change as shown in Figure 3.5. In this figure, we found that at distances of $25 \mu m$ to $275 \mu m$, the S_{21} curve will gradually shift to the right, with a total offset of approximately $0.2 MHz$, at distances of $275 \mu m$ to $425 \mu m$, the S_{21} curve will gradually shift to the left, with a total offset of approximately $0.1 MHz$. The peak values of the S_{21} curve corresponding to the microcavities at different positions only show slight changes, and the maximum difference of the S_{21} curve at the eigenfrequency is only $0.2 dBm$. Therefore, for the convenience of observation, we chose to fabricate microcavities at the centre area of the SAW device.

Finally, we simulated the situation of using the fs Laser cutter multiple times for microcavities preparation at the same point on the SAW device, as shown in Figure 3.6(c). We assume that each laser cutting will increase the depth of the microcavities by $0.1 \mu m$, and the diameter of the microcavities fabricated each time will increase by $10 \mu m$ compared to the previous one, as shown in Figure 3.6(a) and (b). Figure 3.6(a) shows using the fs laser cutter to process microcavities once, while Figure 3.6(b) shows using the laser cutter to process microcavities four times. The advantage of doing so is that it can study microcavities of different diameters

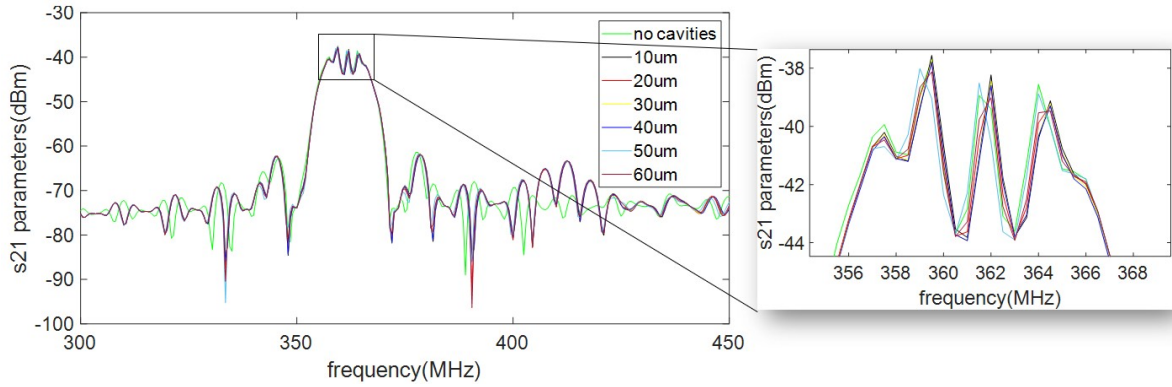


Figure 3.4: Simulated S_{21} parameter of the SAW device with different width microcavities on the substrate.

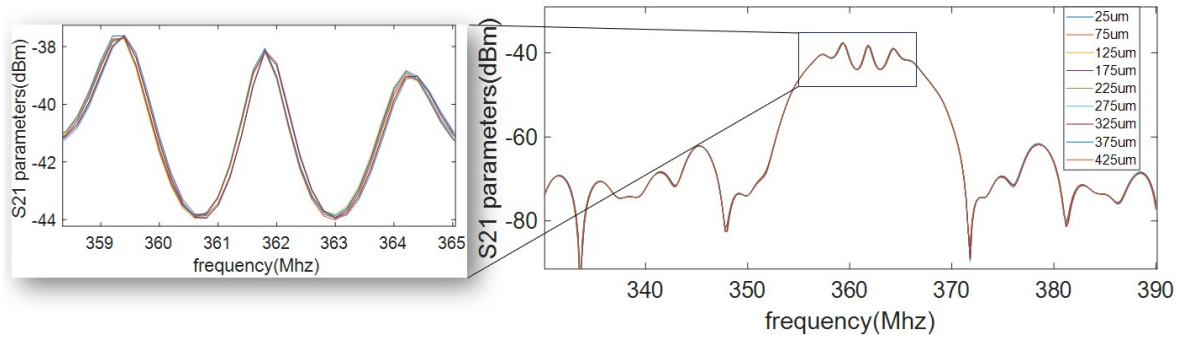


Figure 3.5: Simulated S_{21} parameter of the SAW device with different width microcavities on the substrate.

while avoiding the influence of the SAW reflected between microcavities on the substrate surface. From the simulation results, we found that as the number of the fs laser cutter processing increases, there will be a frequency decrease at the peak of the S_{21} curve of the saw device, each processing will reduce the eigenfrequency by 0.2 MHz , and this means that we need to consider the impact of frequency shift when multiple processing microcavity with the fs laser cutter.

By studying the 2D modal of the SAW device using COMSOL, we simulated the propagation of the SAW near microcavities and its propagation efficiency when propagating the microcavities. Based on the above results, we found that the position and size of microcavities have little effect on the eigenfrequency of SAW devices, but different parameters of microcavities can affect the propagation efficiency of the SAW. After the 2D simulation, we did multiple sets of experiments to obtain the law of the SAW propagation near the microcavities area and suspended membrane.

3.2. S₂₁ Parameter Characterization

Before we actuate the SAW device, we need to find the eigenfrequency of the SAW device. In our experiment, the Vector network analyzer(VNA) has been used to measure the eigenfrequency of the SAW device. Therefore, when the S_{11} parameter is at the lowest point and S_{22} parameter is at the highest point, the reflected energy is the least, the propagated energy is the most, and the amplitude of the excited SAW is largest, the corresponding frequency is the eigenfrequency of the SAW device. The S parameters of the SAW device we used and the SAW device we simulated are shown as Figure3.7 From the measured S_{21} figure, we found that the measured result was not perfectly aligned with the simulation results. We believe that the main reasons for this situation are as follows:

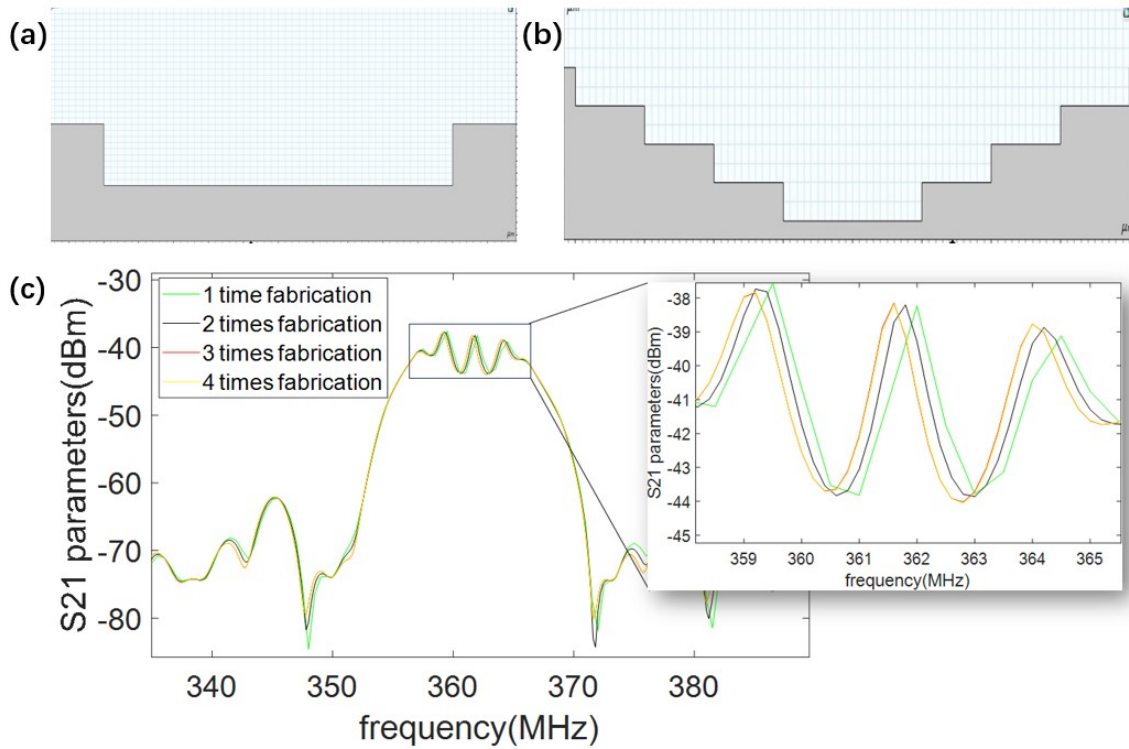


Figure 3.6: (a) Microcavity fabricated by fs laser cutter once. (b) Microcavity fabricated by fs laser cutter four times. (c) Simulated S_{21} parameter of the SAW device with different fabrication times on the substrate.

- During the e-beam writing process of manufacturing, resist material cannot be completely removed as designed, and there will be some errors in subsequent metal evaporation and lift-off process, so there is always a small size error in fabricated interdigital transducers
- As the trial time increases, the SAW device will experience a frequency shift. At the beginning of this project, the eigenfrequency of the SAW device is 381 MHz, and at the end of this project, the eigenfrequency of the SAW device is 385 MHz, as shown in Figure 3.8. This situation may be due to the use of aluminium wires in the wire bonding of the SAW device, which can form an oxide film when exposed to air for a long time, which may affect S parameters. It may also be that prolonged use can cause bumps and wear on the SAW device, thereby affecting S parameters.

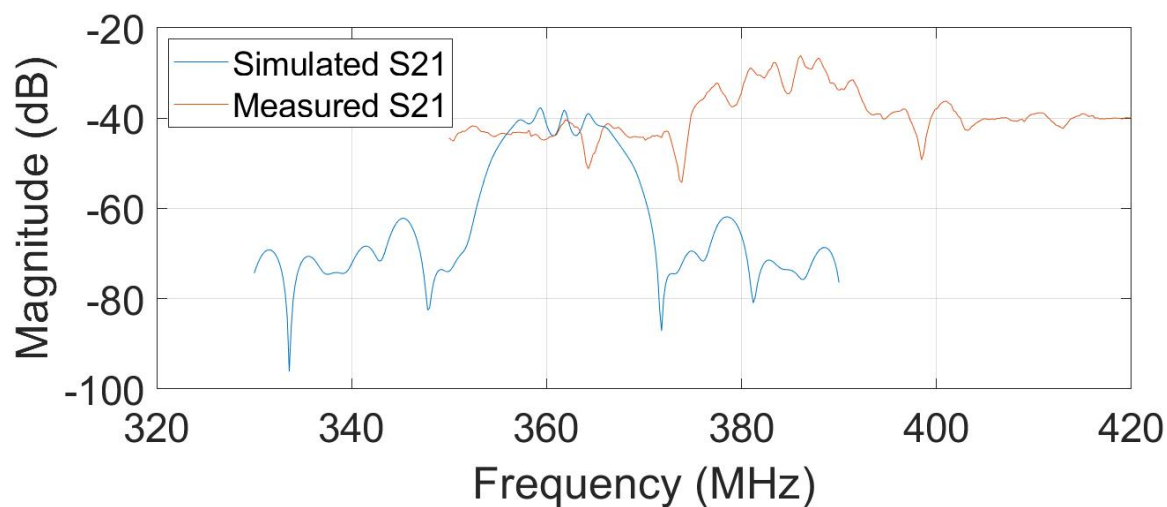


Figure 3.7: S parameter of measured SAW device and simulated SAW device

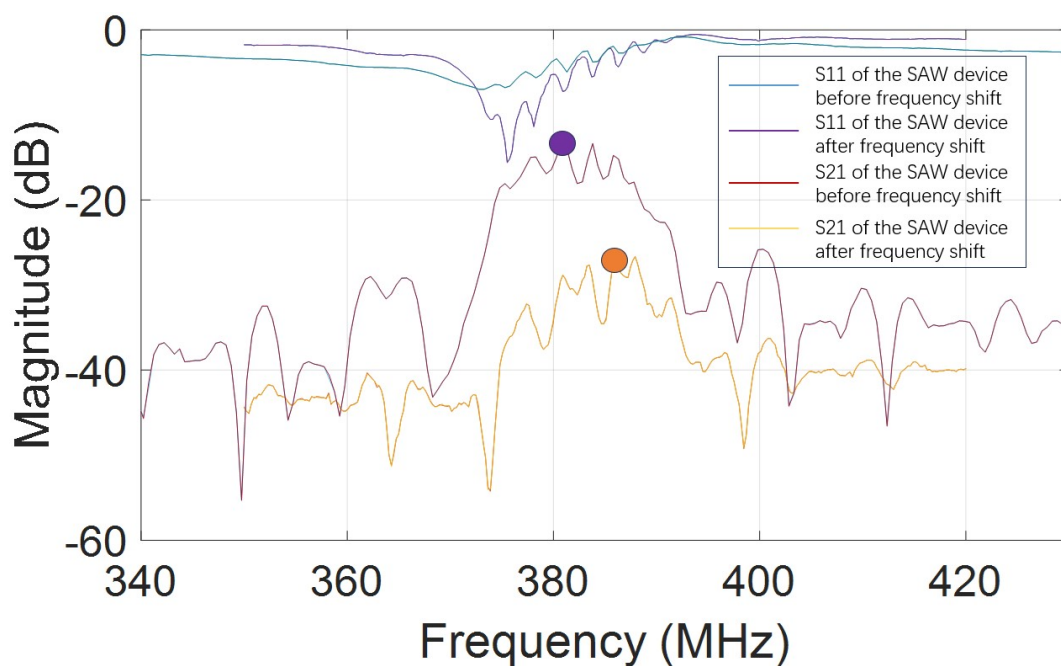


Figure 3.8: S parameter of the SAW device before and after longtime use, the highest point in the S_{21} curve has been represented by ●.

4

Suspended membrane

This project focuses on imaging the SAW field on a suspended membrane; in this chapter, we will introduce how we get the suspended membranes in 3 steps. During the fabrication process, I first fabricated the microcavities and the graphene membranes. After that, I transferred the graphene membranes to microcavities and got the suspended graphene membranes, and finally used two methods to characterise the suspended membrane.

4.1. Microcavities

4.1.1. Fabrication Methods

For microcavities fabrication, there are two main methods: femtosecond(fs) laser cutter etching and focused ion beam(FIB) etching. Laser cutter etching refers to using an ultrashort pulse laser with a pulse width of femtosecond level for etching processing. It uses high-energy beams to illuminate the surface of materials to vaporise them to form line stripping or cutting. The basic principle of FIB is to focus the ion beam on the submicron or even nanometer scale under the action of electric and magnetic fields and control the scanning motion of the ion beam through deflection and acceleration systems. The focused ion beam is directed onto the sample's surface, where it interacts with the material, and the ions(usually gallium) collide with the atoms on the surface, transferring energy to them. During the ion-sample interaction, the ions transfer their energy to the atoms on the sample surface, causing the atoms to be ejected or sputtered away, which effectively removes material from the sample's surface. Comparing these two etching methods, we found that the speed of the fs laser cutter is much faster than that of FIB, but the etching accuracy differs significantly. The processing resolution of the fs laser cutter is about $10\ \mu m$, while the processing resolution of FIB is $10nm$. Considering that the diameter of the microcavities we need is $10\ \mu m$, I decided to use the fs laser cutter to fabricate the microcavities.

4.1.2. Characterization Methods

After completing the fabrication of microcavities, we need to characterise the shape, size, edge morphology, and thickness of these microcavities. In the characterisation process, we use two kinds of instruments to characterise the microcavities, digital optical microscopy and AFM.

For the shape and size characterisation, we used digital optical microscopy, the setup and the characterisation of digital optical microscopy are shown in Figure 4.2 (a). With digital optical microscopy, we can measure the diameter and observe the shape of these microcavities and find how these parameters will affect the size and shape of microcavities.

For the edge topography and thickness characterisation, we used AFM, the setup and the

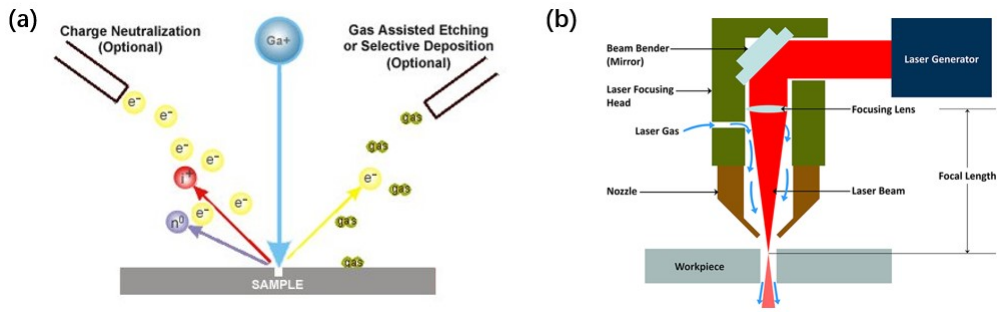


Figure 4.1: (a) Schematic diagram of FIB. (b) Schematic diagram of the fs laser cutter.

characterisation of AFM are shown in Figure 4.2 (b). We use Gwyddion to analyse the data obtained from AFM for the edge topography. During this process, we will draw two intersecting lines in the edge area of the microcavities and preliminarily determine whether the edges satisfy the requirements by changing the height along the lines. If they satisfy the requirements, we will export the height data and use MATLAB to reconstruct the topography of the microcavities to characterise their edge topography.

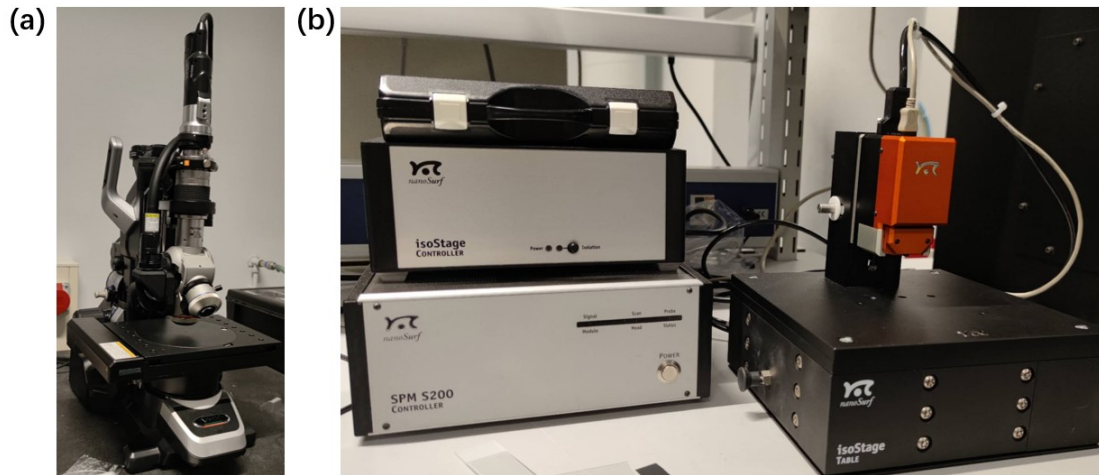


Figure 4.2: (a) Experiment setup of optical microscopy. (b) Experiment setup of AFM.

4.1.3. Fabrication Parameters

We investigated the effects of different fabrication parameters, such as power, jump speed, speed, structure, etc., on microcavities quality in the fabrication process. The meaning of parameters is as follows:

Power: the set laser power [in %]

Jump Speed: The speed of laser scanning before, after, and between laser shots [in mm/s].

Speed: The speed of laser scanning during the laser shot [in mm/s].

Power and Jump speed When exploring the effect of power and jump speed on microcavities, we first draw a matrix on the draft, the power of the fs laser cutter increases from 1% to 10% with the horizontal direction of the matrix and the jump speed of the fs laser cutter increases from 20 to 90 with the vertical direction of the matrix, the diameter of the microcavities on the draft are all $10 \mu m$, the draft and the fabricated matrix are shown in Figure 4.3 (a)

and (b). We characterised the transparent $LiNbO_3$ chip on the glass slide by sticking it with PDMS, and there will be some strange colour in the background due to bubbles between the two materials. From the fabricated microcavities, we find that only when power at 1%, the diameter of microcavities is smaller than the draft. When increasing power to between 2% and 6%, the diameter of microcavities will stabilise at $12 \mu m$. After increasing the power to between 7% and 10%, the diameter of the microcavities will increase again and stabilise at $17 \mu m$. The relationship between the diameter of microcavities and power of fs laser cutter is shown in Figure 4.4(a). After the diameter measurement of microcavities, we studied how the jump speed affects microcavities. We found that the jump speed does not affect the diameter of microcavities, but it affects the shape of microcavities. We found that high jump speed (80 mm/s , 90 mm/s and more) will lead the line trace composed of continuous points in the vertical direction, as shown in Figure 4.4(c).

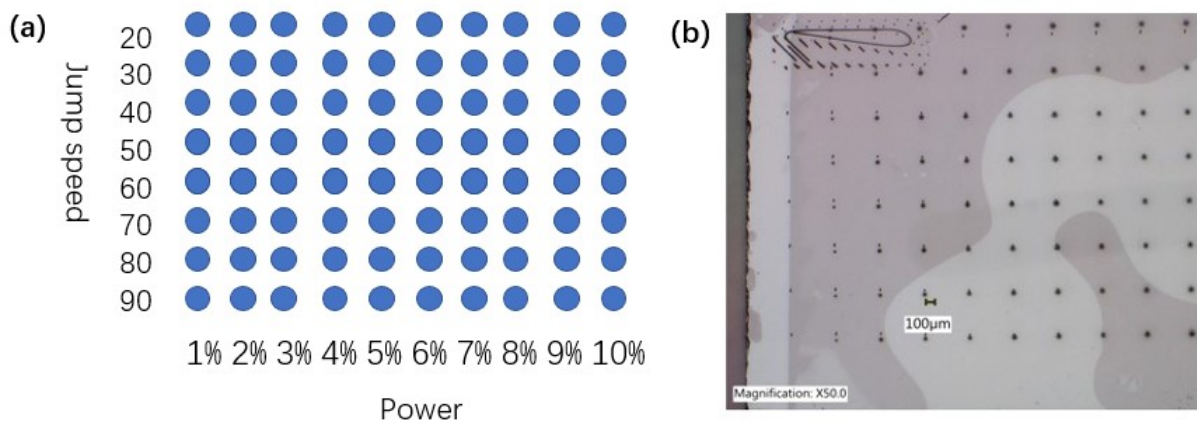


Figure 4.3: (a) Draft of the microcavities matrix. (b) Fabricated microcavities matrix.

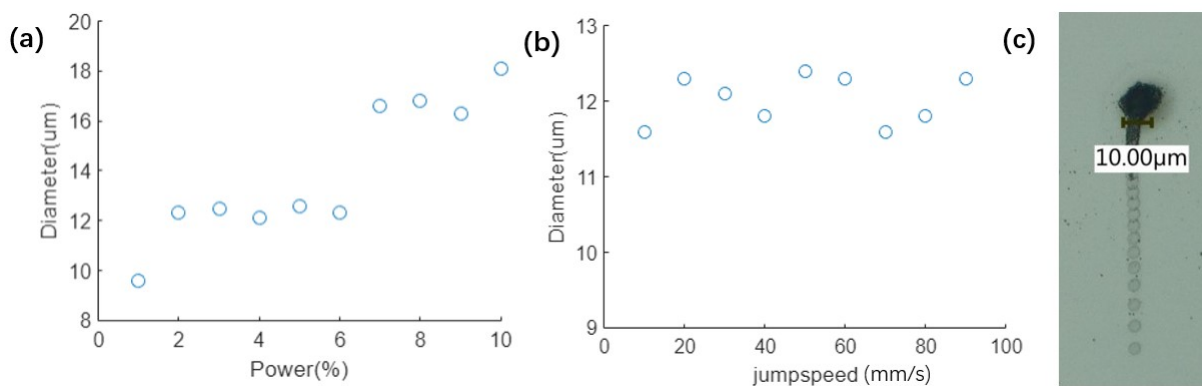


Figure 4.4: (a) Relationship between the diameter of microcavities and power of fs laser cutter when jump speed is 10 mm/s and speed is 100 mm/s . (b) Relationship between the diameter of microcavities and jump speed of fs laser cutter when power is 2% and speed is 100 mm/s . (c) Line trace of microcavities with high jump speed.

Speed When exploring the influence of fs laser cutter parameters on microcavities, we found that changes in the speed of the fs laser cutter can affect the size of microcavities, and the relationship between the diameter of microcavities and the speed of the fs laser cutter is shown as Figure 4.5(a). On the draft of microcavities, the diameter of microcavities is $8 \mu m$, the power and the jumpspeed of the fs laser cutter are 2% and 10, respectively, and the diameter of microcavities decreases with increasing the speed of the fs laser cutter. After the laser speed

increases to 400 mm/s , the diameter of microcavities remains within a constant range under the same other parameters, as shown in Figure 4.5(a).

Structure In the microcavities fabrication process, there are two kinds of structure: point and line. The point means that draw microcavities on the draft and fabricate them one by one, and the line means that draw a rectangle on the draft and fabricate this with the fs laser cutter at high speed. By increasing speed, the fs laser cutter cannot fabricate continuous patterns during etching but instead fabricate intermittent microcavities. With point structure, the edge area of fabricated microcavities is not very flat, which means that the fabricated microcavities are not a very circular shape. With line structure, the shape of fabricated microcavities is better than the microcavities fabricated with point structure; the microcavities fabricated in these two structures are shown in Figure 4.5(b) and (c). However, with line structure, the distance between the microcavities is not controllable; the distance between microcavities is proportional to the speed of the fs laser cutter and ultimately tends to stabilise; the relationship of this is shown as Figure 4.5(d). Considering that too close microcavities distance may affect the transfer of graphene membrane to a specific microcavity, we need to focus on controlling the distance of the microcavity rather than the shape of the microcavity, and we will choose the point structure when manufacturing microcavities.

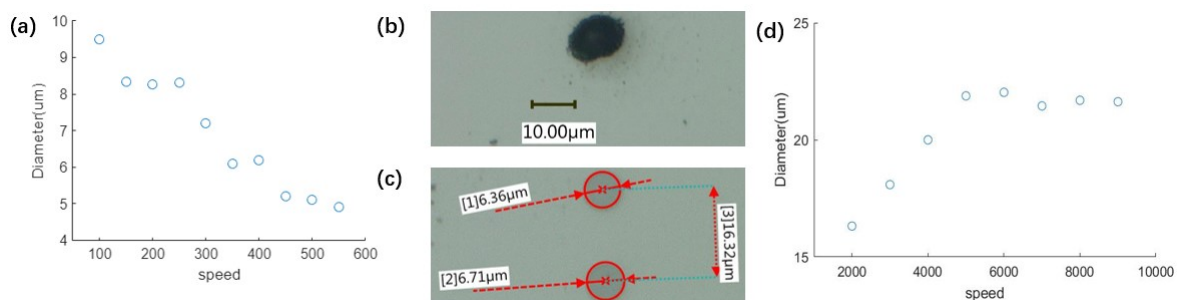


Figure 4.5: (a) Relationship between the diameter of microcavities and speed of fs laser cutter when other parameters keep constant. (b) Microcavities fabricated in the point structure. (c) Microcavities fabricated in the line structure. (D) Relationship between the distance between adjacent microcavities fabricated in line structure and speed of the fs laser cutter when other parameters keep constant

4.2. Graphene Membranes

4.2.1. Thickness characterization

Since the thickness and location of the graphene membrane fabricated by scotch tape are random, we need to detect its thickness and location and select the appropriate graphene flake as our membrane to cover the microcavities. Firstly, we stick the tape with thinner graphene flake to the viscoelastic stamp made of Polydimethylsiloxane (PDMS), use digital microscopy to observe the PDMS with stuck graphene membranes and look for a larger piece of graphene flake under the objective lens with low magnification. Then replace the objective lens with high magnification to observe its thickness and determine its approximate thickness according to its observed colour, as shown in Figure 4.6.

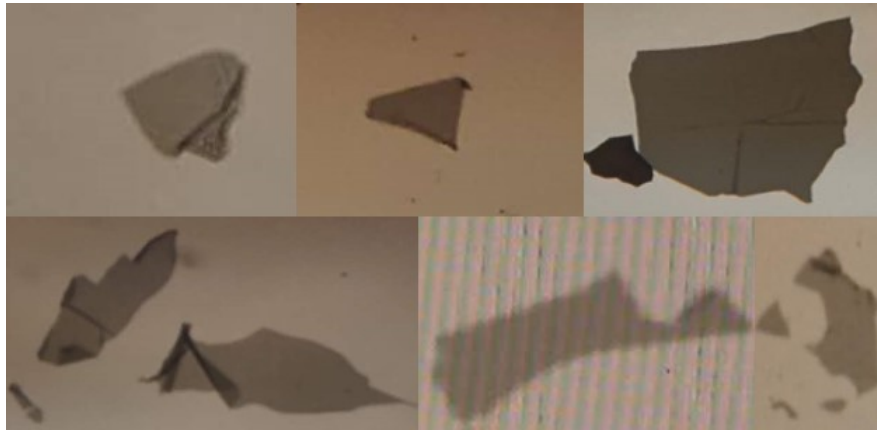


Figure 4.6: Different thicknesses of graphene membranes stuck to PDMS observed by optical microscopy

After transferring the graphene membranes to the substrate, we need to characterise the thickness of the graphene membranes precisely. For accurate characterisation, I used the AFM manufactured by Nanosurf to measure the transferred graphene membranes; the measured topography is shown as Figure 4.7(b). In the measurement process, there will be a slope on the measured area due to the inability to place the sample completely horizontally. We import the height information measured by AFM into MATLAB, calculate the slope of the entire surface, and use the program to remove the slope of the entire surface, reconstructing the surface with graphene membrane and without graphene membrane, as shown in Figure 4.7 (c) and (d). Collect height information of data points in these two reconstructed topography and fit them to the normal distribution curve, the normal distribution curve is shown as Figure 4.7(e).

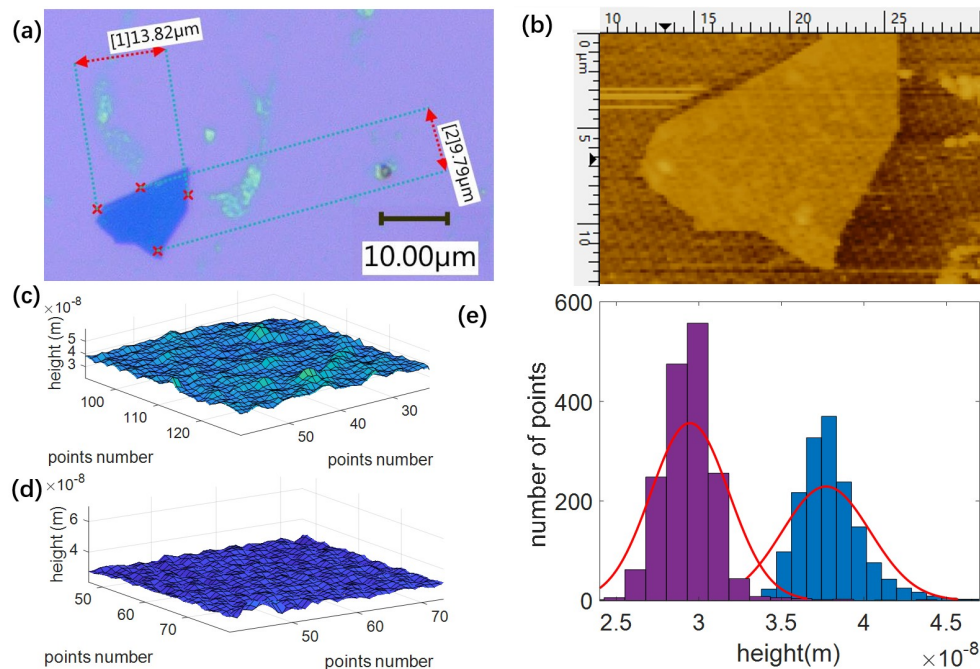


Figure 4.7: (a) Graphene membrane observed by optical microscopy. (b) Topography measured by AFM. (c) Topography of graphene membrane reconstructed with MATLAB. (d) Topography of surface without graphene membrane reconstructed with MATLAB. (e) The height information of the data points in these two topographies and fit them to normal distribution curve

4.2.2. Suspended Membrane Characterization

After we stick our graphene flake to the viscoelastic stamp, we need to transfer the graphene flakes to the microcavities of $LiNbO_3$ to form suspended membranes. In the characterisation of the suspended membranes, we first used an optical microscope to test whether the suspended graphene membrane has been successfully prepared, as shown in Figure 4.8(a), and then used AFM to characterise the suspended membrane, as shown in Figure 4.11(a) and (b), this section will introduce how we image the fabricated suspended membrane with AFM.

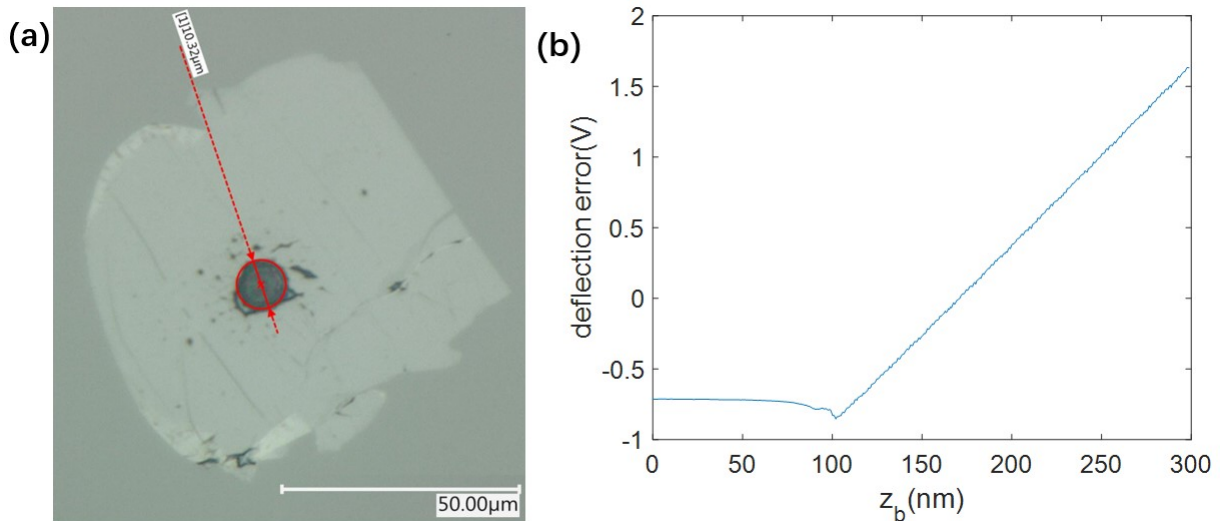


Figure 4.8: (a) Suspended membrane observed using an optical microscope. (b) Deflection versus the change in the cantilever piezo height z_b .

Contact Mode

Contact mode is usually used to characterise the thickness of the graphene flake instead of the graphene membrane because a vertical force will be applied on the measured surface during testing, which can damage the suspended membrane. In 2012, JE Suk et al. measured the topography of ultra-thin membranes at different normal loads using contact mode AFM, and they found that as the vertical load applied by the AFM cantilever increases, the height at the centre of the graphene membrane will decrease, as shown in Figure 4.9 [37].

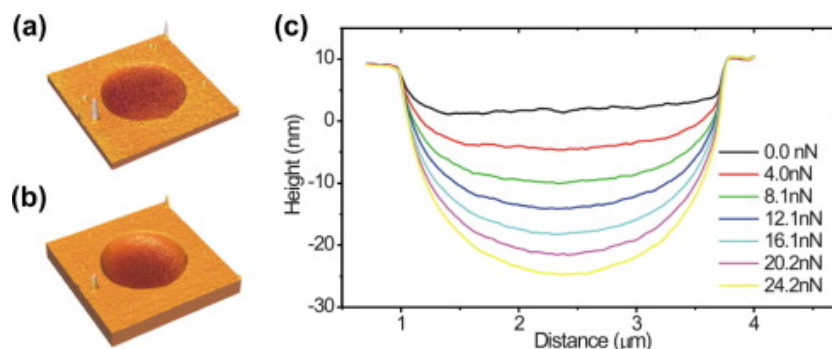


Figure 4.9: (a) and (b) 3D AFM topography images of a 3.7 nm thick a-C membrane at two different loads of 0.0 and 24.2 nN[37]. (c) Cross-sectional line profiles at the centre of the scanned membrane at varying normal loads[37].

In the membrane characterisation, we use Bruker NanoScope V AFM to image the topography of the suspended membrane. During the characterisation, the vertical load is represented

by the setpoint in the panel of scan parameters, and the vertical load can be expressed as follow:

$$F = c * (setpoint - z) * r \quad (4.1)$$

where c is the force constant of the cantilever, z is the initial voltage and r is the cantilever sensitivity. The cantilever sensitivity can be calculated from the slope of the deflection curve, as shown in Figure 4.8(b). Using the cantilever sensitivity, the deflection and deflection error values can be described in units of nm instead of mV . In the measurement process, the AFM cantilever we used is the VTESPA—300 with a spring constant of $40 N/m$ and a resonance frequency of $300 kHz$. We first set a high setpoint($0.3 V$) for the approaching process and measured the deflection versus the change in the cantilever piezo height z_b . The cantilever sensitivity we found is that $r = 0.785nm/mV$. After finishing the approaching process, we decrease the setpoint until $0.02 V$, which can apply a small vertical load($21.9 \mu N$) on the suspended membrane. The measured suspended membrane is shown as Figure 4.10(a).

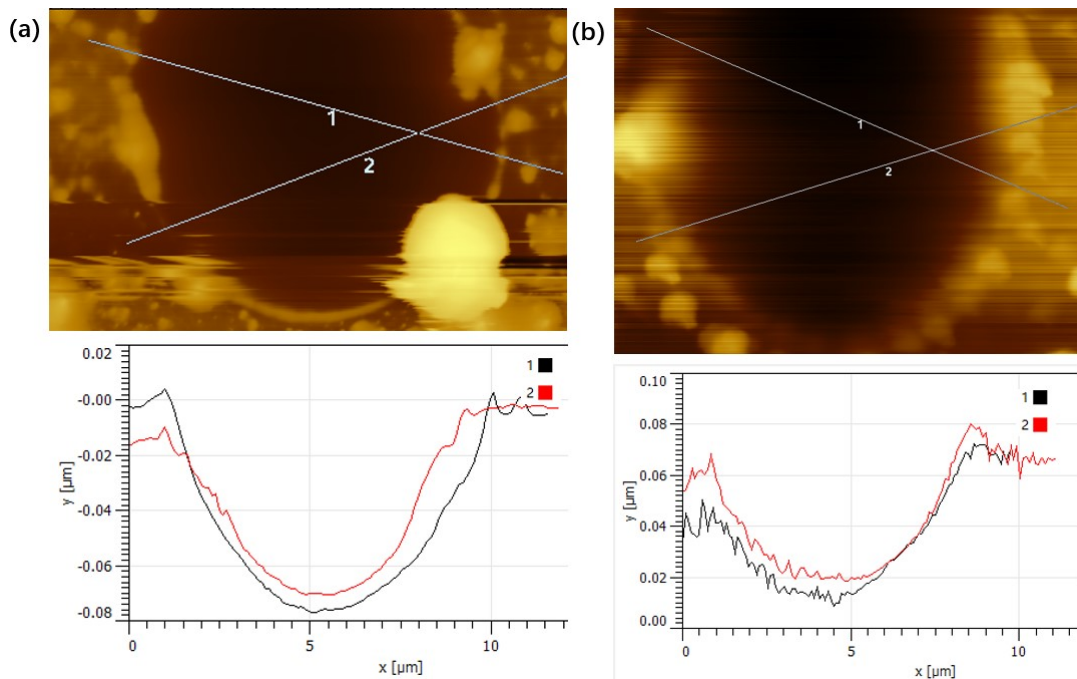


Figure 4.10: (a) Topography of the suspended membrane measured in contact mode. (b) Topography of the same suspended membrane measured in tapping mode

Tapping Mode

In Tapping mode, we changed the cantilever and tuned the AFM cantilever. After that, we measured the topography of the suspended membrane in tapping mode, as shown in Figure 4.10(b). From Figure 4.10, we found that the depth of the depression measured in contact mode is $70 nm$ and that measured in tapping mode is $35 nm$. It can be seen from the depression depth under two different measurement modes that the application of vertical load will cause the depression of the suspended membrane to become deeper, which is consistent with the research results of JE Suk et al. in Figure 4.9.

After we fabricated the transfer process, we found that the graphene membranes above the microcavities would have a protrusion or a depression, and the probability of depression is much greater than that of protrusion. In the characterisation of the protrusion and depression, we first processed the topography measured by AFM with Gwyddion and collected the data

from the topography. After that, we imported these data into MATLAB and used them to reconstruct the surface morphology to determine the height gap of the depression and protrusion, as shown in Figure 4.11(a) and (b).

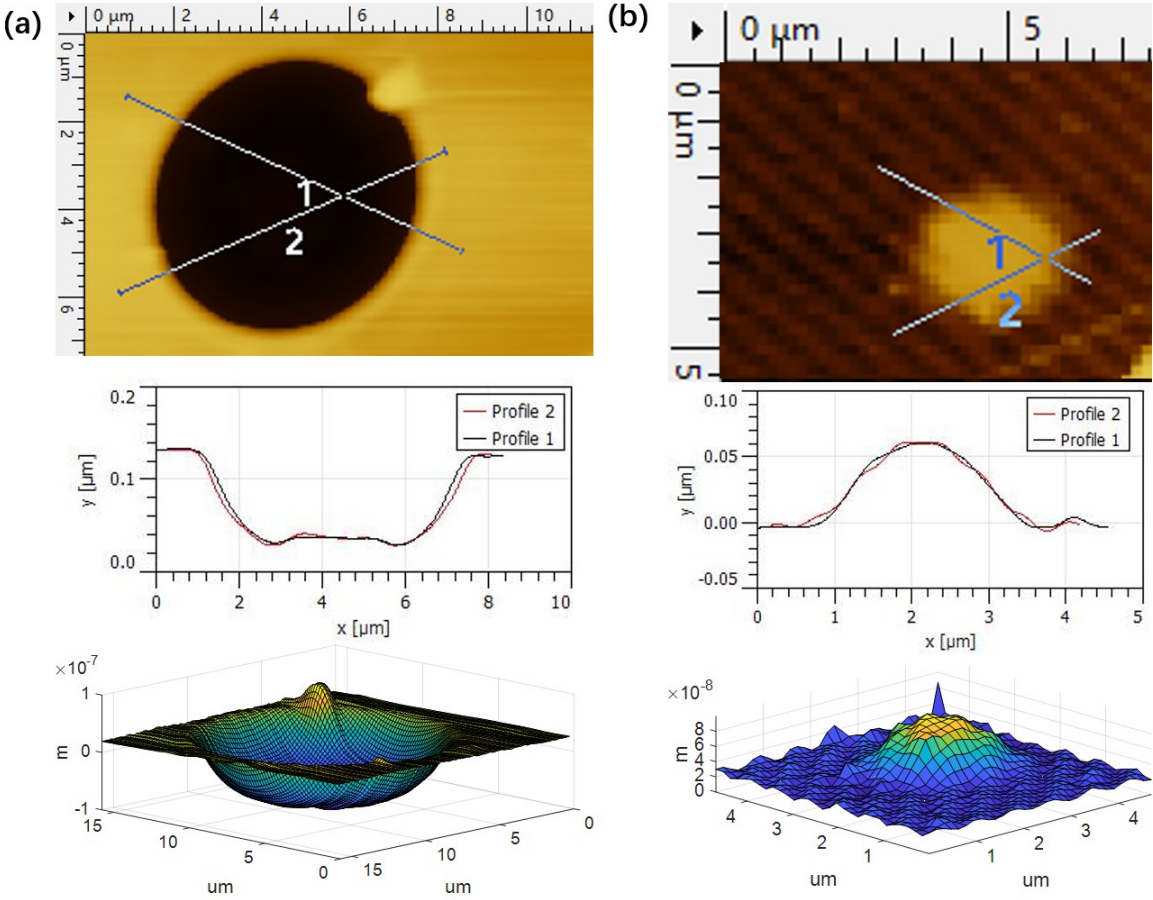


Figure 4.11: (a) The topography and axonometric Figure of the suspended membrane with depression. (b) The topography and axonometric Figure of the suspended membrane with protrusion.

5

Direct Imaging

In this project, we chose two image methods to image the SAW field, direct imaging and contact imaging. In direct imaging, we use DHM to image the SAW field and combine the amplitude modulation(AM) and stroboscopic unit to image the SAW field. In contact imaging, we use AFM to image the SAW field and combine the amplitude modulation and AFM to image the SAW field.

At first, we tried to use DHM to image the SAW field on the SAW device substrate. The period of the SAW is much shorter than the shutter time of the high-speed camera, and we developed some imaging methods that can increase the measured frequency of DHM: stroboscopic effect, frequency modulation, and amplitude modulation.

5.1. Methods to increase the measured frequency of DHM

5.1.1. Stroboscopic Effect

A shutter speed parameter will be set when we use the camera to take pictures. The same is true for DHM, which will have the shortest shutter opening time when recording wavefront information. This will limit the vibration frequency on the measured surface, and we can use the stroboscopic effect to improve the range of vibration frequency that DHM can measure. The stroboscopic effect is a visual phenomenon caused by aliasing when a rapidly flashing light source is synchronized with the object's motion, the object or process appears to be moving in slow motion or appears to be still. The stroboscopic effect is a valuable tool for studying high-frequency vibrations, as it provides a way to visualize and analyze motion that would otherwise be too rapid to observe directly. We can use a stroboscopic unit to generate the input signal and control the illumination system, the working principle of the stroboscopic unit is shown in Figure 5.1(a). The stroboscopic mode opens the shutter time to milliseconds, but the illumination only comprises a few laser pulses superimposed on one image. In fact, to achieve high-frequency analysis for the SAW device, a pulse shorter than the minimum shutter time of the camera is required. There will be several laser pulses on one camera frame with a duration as low as $0.0075 \mu s$. Each pulse is precisely given at the same phase during the excitation period. Once a frame is captured, the pulse of the second frame moves slightly during the cycle, with a movement period of 0.1 vibration period during the experiment.

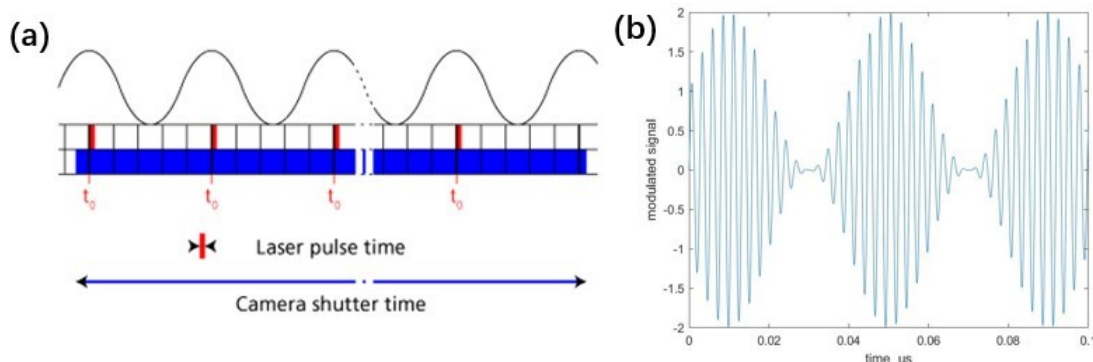


Figure 5.1: (a) Stroboscopic acquisition principle. (b) Amplitude modulation of 381 MHz input signal of SAW device and 25 MHz carrier signal.

In the experiment, we use the stroboscopic unit manufactured by Lyncée Tec to achieve the stroboscopic acquisition. The stroboscopic unit is connected to the test device, and the signal is sent as an output signal to the test device. The signal from the stroboscopic unit is also sent to DHM to control the opening and closing of the pulse illumination source of DHM to achieve stroboscopic acquisition.

To verify that the experimental setup for stroboscopic acquisition can work, we use DHM with the stroboscopic unit to measure the vibration of a piezo. The piezo's frequency response plot is shown as Figure 5.2, which is measured by Polytec MSA400 laser Doppler vibrometer. We found two peaks in this plot, meaning there are two resonance frequencies of this piezo, 3.1 kHz and 4.8 kHz respectively. During the testing, we chose a 5kHz signal as the input

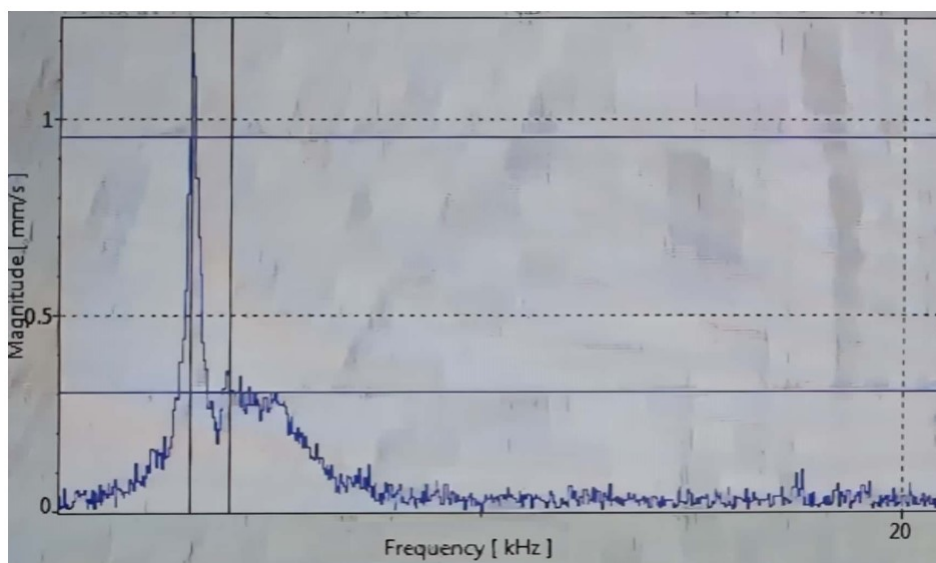


Figure 5.2: Frequency response plot of used piezo

of the piezo, which means that the surface vibration period is shorter than the shutter time, and the CCD sensor cannot record the vibration of the Piezo surface. In the experiment, we set the input frequency of piezo as 5 kHz and the power as 10 dBm. At first, we turned off the power of the stroboscopic unit and used DHM to image the piezo directly. After we heard the voice generated by the piezo, which means it started vibration, we chose 4 points on the piezo surface randomly and recorded their motion, and the recorded result is shown in

Figure 5.3(a). From Figure 5.3(a), we found that the motion trajectories of these five points are irregular, which contradicts the result that Piezo should vibrate at a frequency of 5 kHz . After that, we powered on the stroboscopic unit, set the output of the stroboscopic unit as the input of the piezo, the frequency of the signal was 5 kHz , and the power was 10 dBm , used the stroboscopic mode of DHM to image the piezo, we use the 4 points on the piezo surface chosen before and recorded their motion, the recorded result is shown in Figure 5.3(b). From Figure 5.3(b), we found that the motion tracks of these 4 points seem to can be fitted into periodic function, and the period of these motions is 0.2 ms . By comparing the motion tracks applying and without applying stroboscopic mode, we preliminarily verified the feasibility of the stroboscopic effect in measuring the vibration in which the movement period is shorter than the shutter time of the CCD sensor.

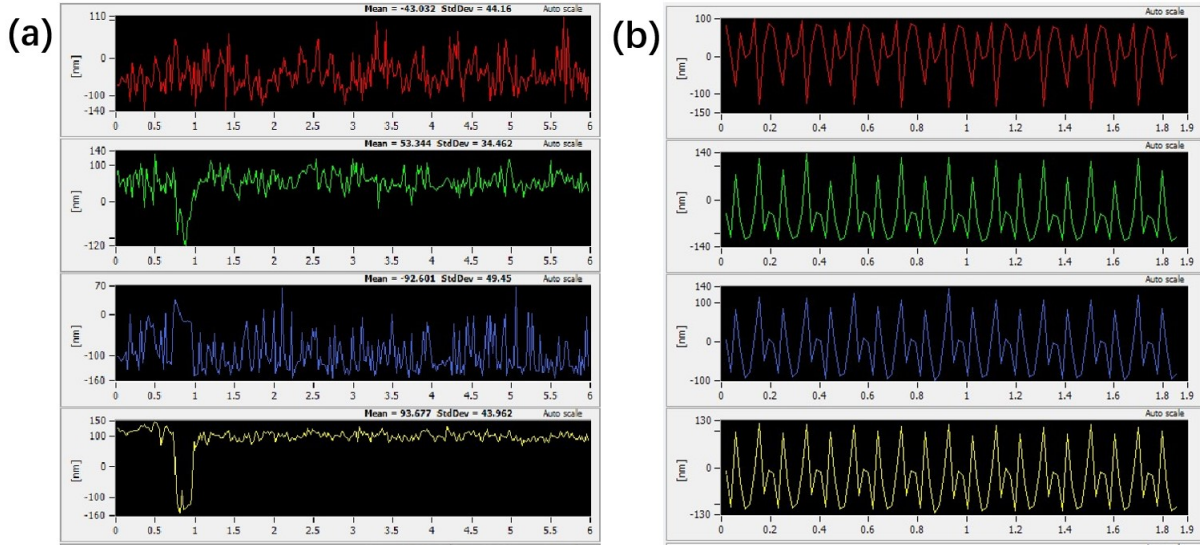


Figure 5.3: (a) Motion trajectories of 5 points of Piezo recorded by CCD sensor. (b) Motion trajectories of 5 points of Piezo recorded by CCD sensor and stroboscopic unit.

5.1.2. Amplitude Modulation

Amplitude modulation (AM) is a modulation technique used for transmitting messages with a radio wave. In amplitude modulation, the amplitude of the signal wave is varied in proportion to that of the carrier wave. The mathematical analysis of AM is shown as follows:

The carrier wave (sine wave) of frequency f_c and amplitude A is expressed by

$$c(t) = A * \sin(2\pi * f_c * t) \quad (5.1)$$

The message signal, such as a generator signal that is used for modulating the carrier, is $m(t)$ and has a frequency f_m

$$m(t) = M * \cos(2 * \pi * f_m t + \phi) = Am * \cos(2 * \pi * f_m t + \phi) \quad (5.2)$$

In this equation, m is the amplitude sensitivity which equals to $\frac{M}{A}$ and M is the amplitude of modulation. Amplitude modulation results when the carrier $c(t)$ is multiplied by the positive quantity $(1 + m(t)/A)$:

$$y = (1 + m * m(t)). * c(t) \quad (5.3)$$

In this project, we set f_c as the carrier signal frequency and f_m as the frequency of our SAW device, which is 25 MHz and 381 MHz , respectively. In the control panel of the signal generator, we set the amplitude of the SAW device as the same as that of the carrier signal, which means that the amplitude sensitivity is 1, and the modulated signal is shown in Figure 5.1(c). To verify that the experimental setup can measure the high-frequency vibration with amplitude modulation, we used the piezo used in the last subsection to do the test, the experimental setup is shown in Figure 5.4. The stroboscopic unit is connected to the signal generator, and the signal from the stroboscopic unit will be modulated internally in the signal generator and sent as an output signal to the SAW device. The signal from the stroboscopic unit sent to DHM will control the opening and closing of the pulse illumination source of DHM to achieve stroboscopic acquisition while achieving synchronous output with the signal generator. In the

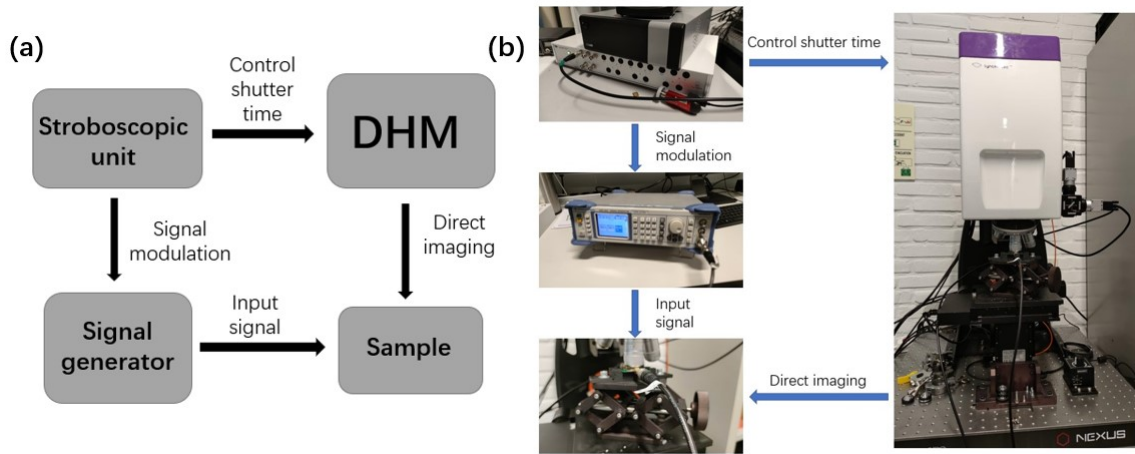


Figure 5.4: (a) Schematic diagram of the experimental equipment. (b) Experiment setup of DHM imaging, from top to bottom on the left are stroboscopic unit, signal generator, and SAW device, while on the right is DHM.

verification process, we first do the amplitude modulation for the input signal, we set the frequency of the stroboscopic unit as 0.5 kHz , the frequency and the power of the signal generator as 5 kHz and 10 dBm respectively, and the modulated signal is shown as Figure 5.5(a). In the DHM recording process, the CCD sensor records the instantaneous position of a point within each shutter time, with a phase interval of 0.2π between adjacent shutter times. Therefore, every ten frames can fully record the vibration situation of the point within one period. The laser pulse time of the illumination source is $0.0075\text{ }\mu\text{s}$, much smaller than the piezo's vibration period. Therefore, we assume that the points on the surface are stationary during a single laser pulse. In Matlab, we set the phase difference of each pulse as 0.2π , and the result of the stroboscopic acquisition modulated signal is shown in Figure 5.5(b). In this figure, the red line is formed by sequentially connecting the acquisition points, and the blue line is the simulated signal. From this figure, we find that after pressing the red line 110 times along the x-axis, the acquisition wave (red) can be mostly fitted with the blue line.

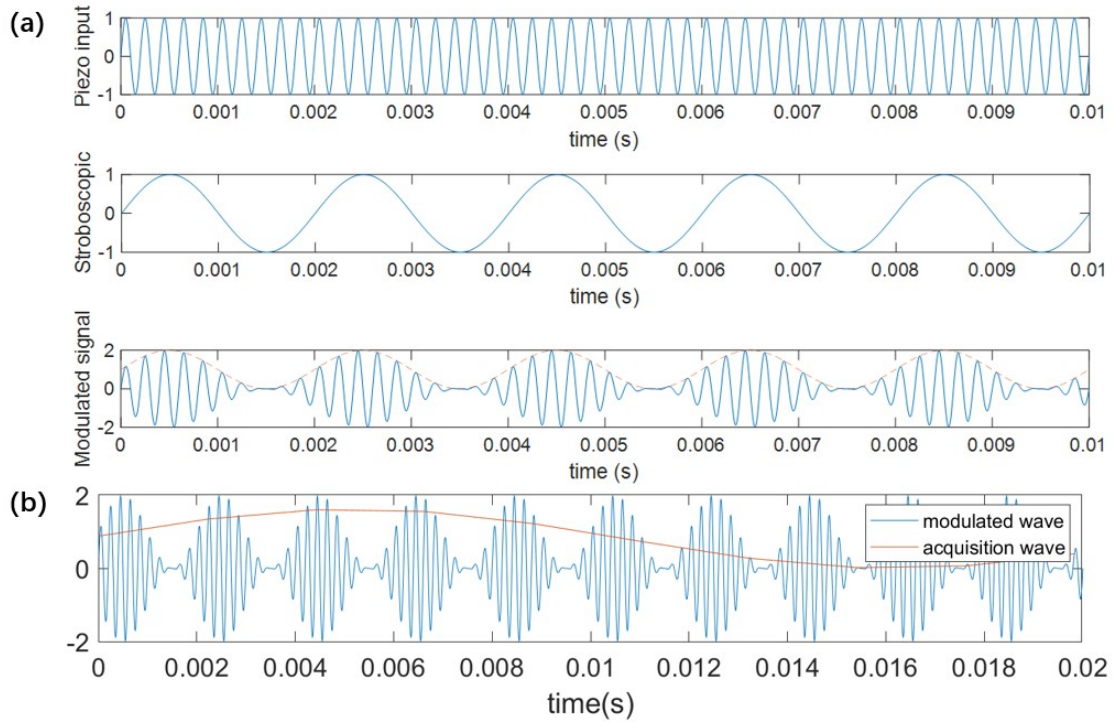


Figure 5.5: (a) Input signal after amplitude modulation of the piezo. (b) Simulation of the acquisition process of piezo.

Based on the above results, we conducted experiments on stroboscopic acquisition. We first set the output frequency of the stroboscopic unit to 5 kHz , sent the output to the piezo, and observed the motion trajectory of the piezo surface. Then we set the output of the stroboscopic unit to 0.5 kHz and connected its output to the signal generator. The modulation signal generated by the signal generator serves as the input of the piezo and records the motion trajectory of the same point on the piezo surface in both normal mode and stroboscopic mode. Finally, comparing the two trajectory maps obtained, the result is shown in Figure 5.6. The red line is the motion trajectory collected in the stroboscopic mode without AM, and the green line is the motion trajectory collected in the stroboscopic mode with AM signal. We found that after stretching the time axis 11 times the vibration information collected in stroboscopic mode with AM, the motion trajectory can fit well with that collected in the stroboscopic mode without AM, so we believe that this experimental setup can measure the high-frequency vibration with amplitude modulation.

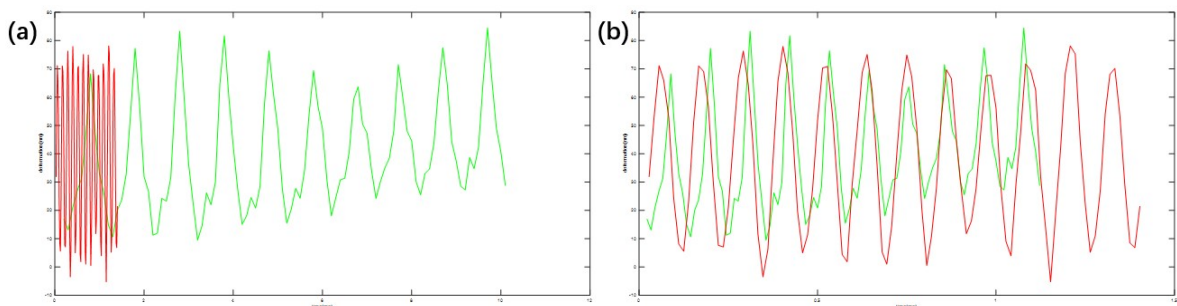


Figure 5.6: (a) Collected vibration information of piezo surface in stroboscopic mode with AM (green) and without AM (red). (b) Comparison of vibration information collected on the Piezo surface with AM after stretching 11 times axis with that without AM.

5.2. Measurement With DHM

In the characterization of the SAW field, we first connected all the cables of the instrument and set parameters. In the parameters setting of amplitude modulation, we set the frequency of the carrier signal as 381MHz, the frequency of the message signal as 12.7 MHz and the power of the modulated signal as 10dBm, the modulated wave is shown as Figure 5.7(a).

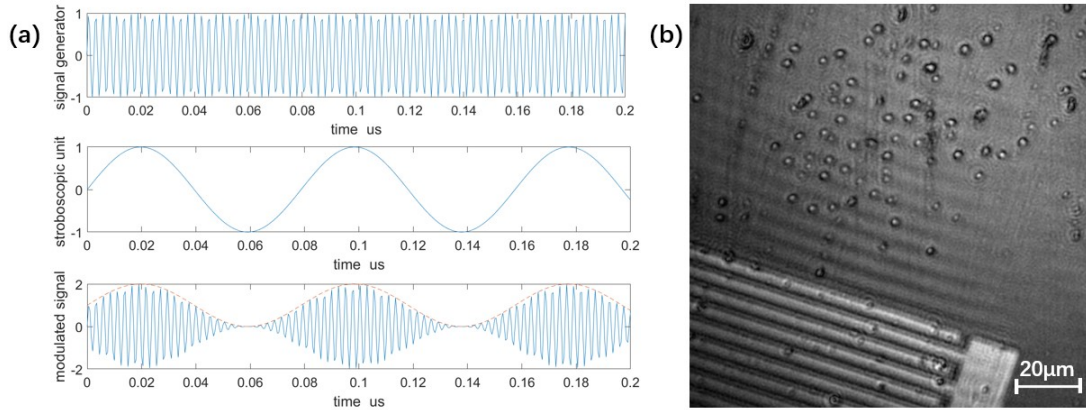


Figure 5.7: (a) Modulated signal with 381 MHz signal generator signal and 12.7 MHz stroboscopic unit signal. (b) Area trying to image the SAW field.

In the measurement process of the SAW field, we first tried to measure the whole field. We use DHM to image an area which has a standing SAW field on the surface and use the modulated signal to activate the SAW device, and the observed area is shown in Figure 5.7(b). We can see that in this figure, there are obvious alternating light and dark patterns near IDTs, and the intensity of the light and dark patterns decreases as the distance from IDTs increases. We think that this situation is caused by insufficient input signal power, and we increase the power of the output of the signal generator from 10 dBm to 23 dBm, which is the maximum output that can be generated at this frequency. After trying different inputs, the measured patterns are still the same, we believe that other reasons cause this situation and the field we observed is not the SAW field. To verify this assumption, we cut off the SAW device's input and find that the image of this field is the same as the image of the SAW device with input in Figure 5.7(b), which confirms that this situation is independent of the input. After that, we observed another SAW device, and the area near its IDTs is shown in Figure 5.8(a) and (b), we found that the situation that appeared in the SAW device before also appeared in this SAW device. Then we use DHM to image IDTs integrated on Si substrate, which is a nontransparent material, the observed image is shown in Figure 5.8(c) and (d). It was found that although (c) and (d) were nontransparent substrates, the previously mentioned light and dark patterns also appeared.

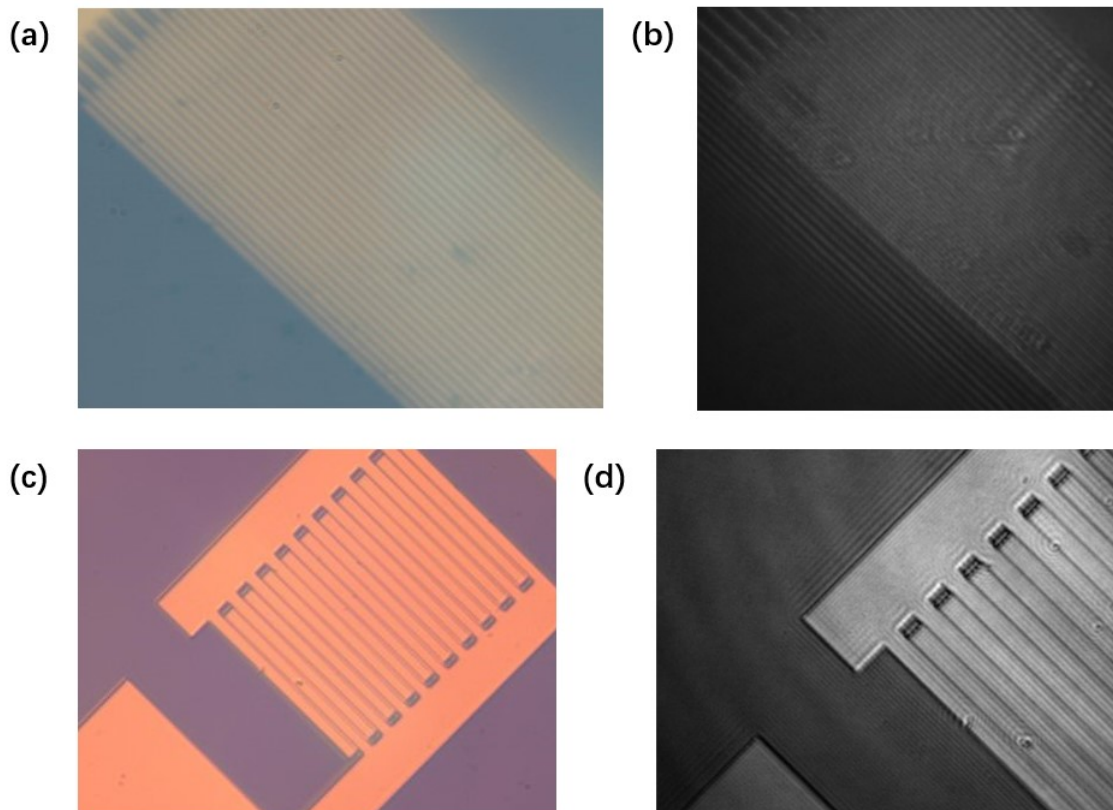


Figure 5.8: (a) IDTs and their surrounding areas on another SAW device observed by optical microscope. (b) IDTs and their surrounding areas on another SAW device observed by DHM. (c) IDTs and their surrounding areas on the SAW device with silicon substrate observed by optical microscope. (d) IDTs and their surrounding areas on the SAW device with silicon substrate observed by DHM.

From Figure 5.9, there are two types of interference stripe noise here, one is the coarse interference stripe marked with yellow and green, and the other is the fine interference stripe marked with blue and purple. We believe that the above situation may be caused by reason as follow:

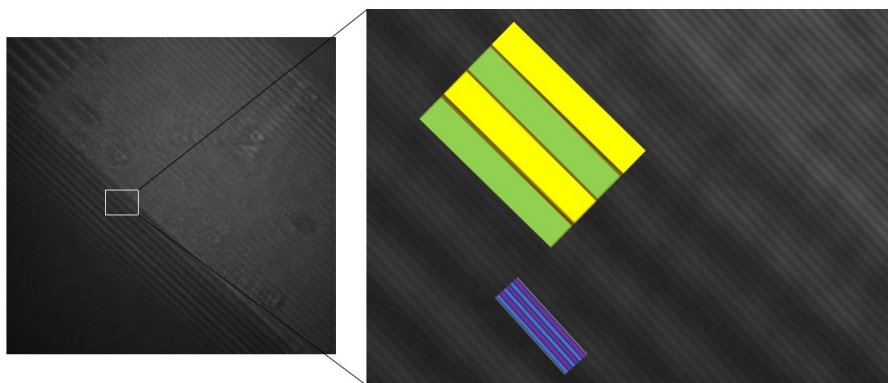


Figure 5.9: Two kinds of interference stripe noise on another SAW device

- **Noise:** During the recording process of a digital holographic measurement system, when a laser is irradiated on a rough surface, due to the high coherence of the laser, the scattered light from the edge of the IDTs interferes with the scattered light generated by the substrate,

resulting in a regularly distributed stripe pattern. The principle of generating stripe patterns is shown in Figure 5.10. After excitation of the standing SAW field, the height of points on the line perpendicular to the propagation direction of SAW is the same in the centre of the SAW device. Therefore, we assume that there is a scattering line source at the edge of the IDTs, and the scattering line source $q(x, y_i)$ from the scattering surface scatters onto the receiving surface, the complex amplitude of the elementary light wave at the receiving point P can be expressed as:

$$E_i(P) = a(x, y_i) \exp[j\phi R(x, y_i)] \exp[j\phi(r)] \quad (5.4)$$

In the formula: $a(x, y_i)$ represents the amplitude of the reflected light from the scattered surface; $R(x, y_i)$ represents the random phase introduced by the roughness of the scattering surface; $\phi(r)$ represents the phase of light propagation. The complex amplitude in point P is the superposition of N independent scattering line sources propagating light waves to that point. Therefore, the intensity of the point P speckle can be expressed as:

$$I(P) = |E(P)|^2 = \left| \sum_{i=1}^N a(x, y_i) \exp[j\phi R(x, y_i)] \exp[j\phi(r)] \right|^2 \quad (5.5)$$

Because $a(x, y_i)$ and $R(x, y_i)$ both vary along the arrangement direction of the IDTs array, the distribution of complex amplitude $E(P)$ on the receiving surface also varies along that direction. For different reference points, the distribution of light intensity varies with the array of distance IDTs, resulting in a pattern of bright and dark stripes. In the process of DHM recording, the intensity formula of the interference between object beam $O(x, y)$ and reference beam $R(x, y)$ can be expressed as:

$$I(x, y) = |O(x, y)|^2 + |R(x, y)|^2 + O^*(x, y)R(x, y) + O(x, y)R^*(x, y) + I(P) \quad (5.6)$$

The first two are intensity distributions of the object beam and the reference beam, which are only related to the amplitude, $I(P)$ is the intensity change caused by noise, and this is the reason for the appearance of light and dark stripes.

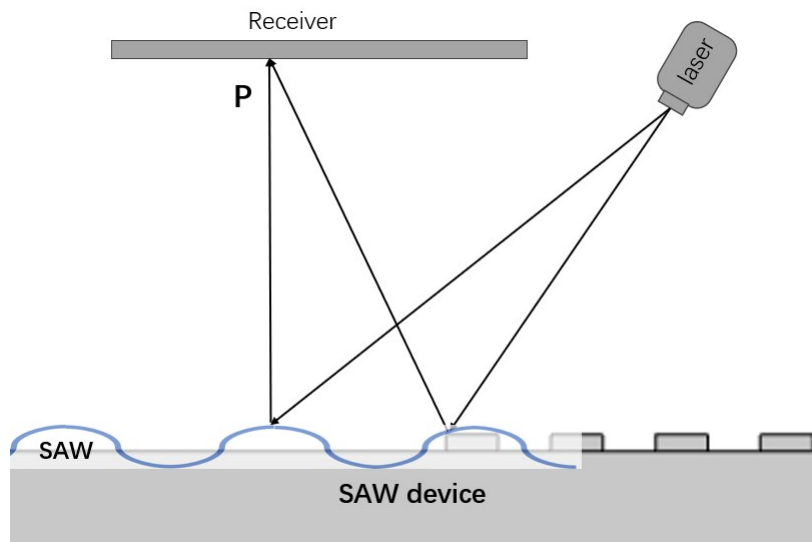


Figure 5.10: The principle of generating stripe patterns.

Then we tried to measure the changes in some points on the SAW device surface, in the measurement process, we chose 5 points along the direction of SAW propagation. We set

the frequency of the carrier signal as 381 MHz , the frequency of the message signal as 12.7 MHz and the power of the modulated signal as 5 dBm , We first chose 3 points on the surface of the SAW device and used the stroboscopic mode of DHM to image the SAW field on the surface, the position of measured field and the measured result is shown as Figure 5.11 (a) and (b) respectively. From this figure, we can not get any useful information and the vibration of the surface seems random. Then we increased the power of the signal generator and stroboscopic unit from 5 dBm to 23 dBm (maximum), the measured result is shown as Figure 5.11(c). However, after increased input power, the height variation still looks messy and disorganized, and the height amplitude seems too small, which may be the noise from the surrounding environment. To verify the assumption about the noise, we used the DHM to measure these 3 points without an input signal, as shown in Figure 5.12(a). The height vibration information is very similar to the previous two images, so we believe that we did not collect available position information when measuring these points.

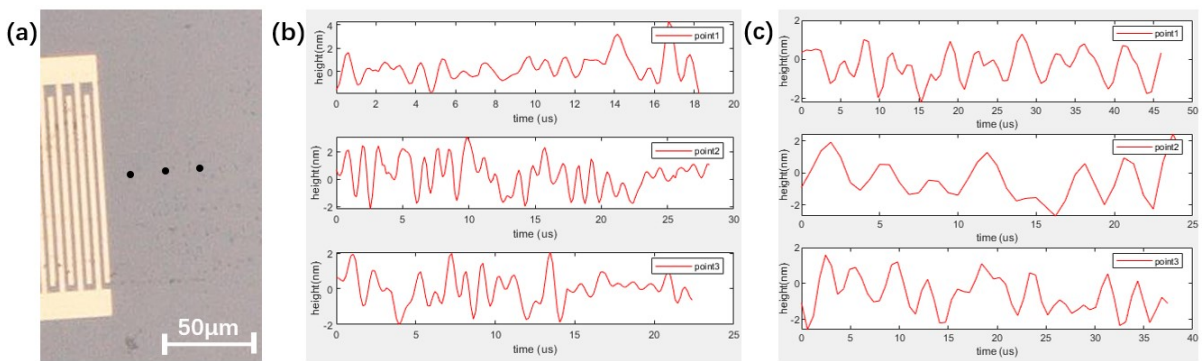


Figure 5.11: (a) Position of three measured points, from left to right, it is point 1, point 2, and point c in sequence. (b) Heights of three points on the SAW device change with time at low power input. (c) Heights of three points on the SAW device change with time at high power input.

5.3. Failure Reason

After conducting multiple repeated experiments, we were still unable to image the SAW field successfully, the reason for the failure is as follows:

The amplitude of the saw field is too small, we simulate the SAW device with an input power of 23 dBm and frequency of 362 MHz , which is the simulated eigenfrequency, and the amplitude of SAW is 2.2 nm . Although it is higher than the resolution of DHM (0.3 nm), we found significant noise during measurement, approximately 2 nm , as shown in Figure 5.12 (a), which is close to the maximum amplitude we can excite SAW and have an impact on the measurement. In summary, we believe that the small amplitude of the SAW field is the main reason for the failure of DHM imaging.

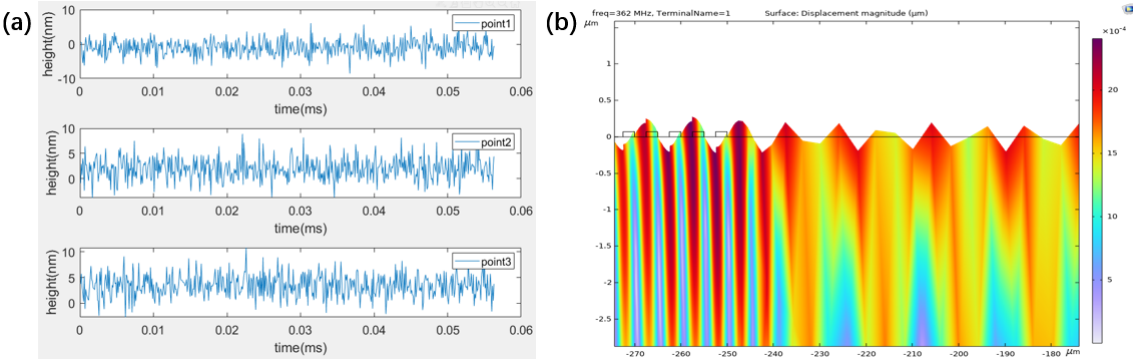


Figure 5.12: (a) Noise(measurement of a flat and stationary surface) of DHM during the measurement process. (b) Simulation of the SAW device with input 23dbm and frequency 362MHz .

6

AFM Imaging

In this chapter, we use AFM to image the SAW field after we do not get the SAW field image by using DHM. In the AFM imaging process, we will divide the imaging part into three parts: image the SAW field on the SAW substrate, image the SAW field on the surface with microcavities, and image the SAW field on the suspended membranes.

6.1. Setup of the SAW Field Imaging

In the SAW field imaging experiment, the schematic diagram of the experimental setup is shown as Figure 6.1(a). We use an RF signal generator to generate the RF signal around the SAW device's eigenfrequency, set the lock-in amplifier's reference signal as the carrier signal to modulate the RF signal and set the modulated signal as the input of the SAW device. The cantilever of AFM will deflect due to the SAW field on the surface of the SAW device, and the lock-in amplifier will collect the signal at its reference frequency, the software will process the output of the AFM and lock-in amplifier to generate the topography of the SAW device and the amplitude map of the SAW field respectively.

In the experiment, the RF signal was generated and modulated by the Rohde & Schwarz

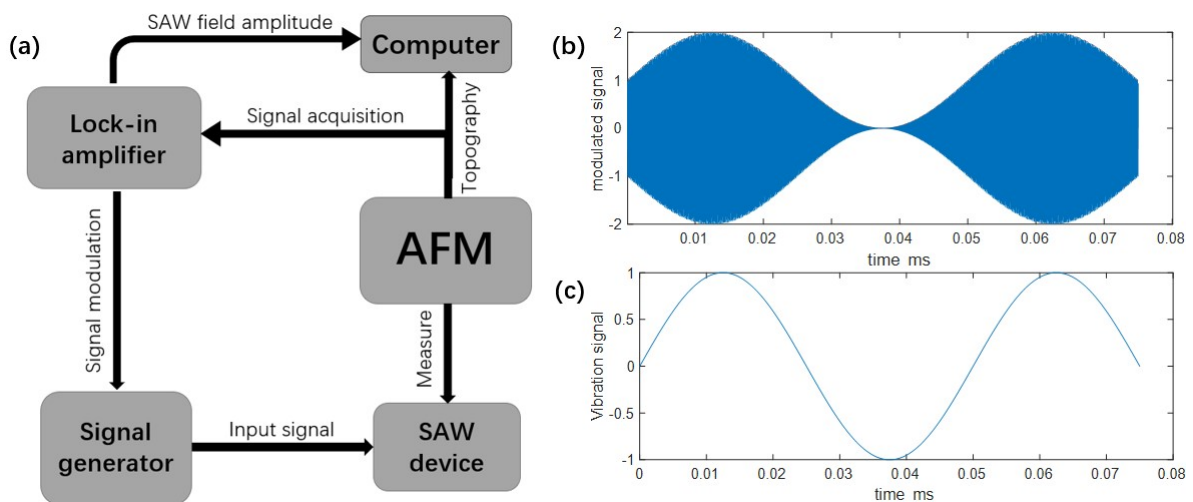


Figure 6.1: (a) Schematic diagram of the experimental setup for SAW field image. (b) Modulated signal for the SAW device. (c) Obtained vibration signal about a certain point.

SMB 100B Signal Generator, the SAW field was imaged by the Bruker NanoScope V AFM and the reference signal of built-in lock-in amplifier was used as carrier signal in the AM process.

The frequency of the reference signal of the built-in lock-in amplifier was set as 20 kHz , and the modulated signal is shown as Figure 6.1(b), which means that there is a high-frequency standing wave field ($\approx 380\text{ MHz}$) on the surface of the SAW device and the amplitude of this standing wave field exhibits periodic changes ($= 20\text{ kHz}$), the periodic change of amplitude for a certain point is shown as Figure 6.1(c). The periodic change of cantilever deflection was recorded by the built-in lock-in amplifier, the deflection of all the scanned points was collected, and the standing SAW field was measured.

6.2. Imaging the SAW field on the SAW device substrate

In this part, we use AFM to image the SAW field propagated by the SAW device substrate. We imaged the SAW field in different frequencies and powers, and the imaged SAW field is shown in Figure 6.2(a). Then we use Matlab to rebuild the surface of the SAW field, as shown in Figure 6.2(b) and (c). In Figure 6.2(c), we use shaded areas to label the peak areas of the SAW field and black border areas to label the valley areas of the SAW field, then calculate the average value of these two kinds of areas and fit their height information into a normal distribution curve, as shown in Figure 6.2(d). By calculating the difference between the centre of two curves in Figure 6.2(d), we can obtain the amplitude of SAW and study the relationship between the SAW field amplitude and the driving frequency and the input power of the SAW field through this method. In Figure 6.2(d), the amplitude (height difference between two curves) is 2.67 mV , according to equation 4.1, the amplitude should be 2.09 nm .

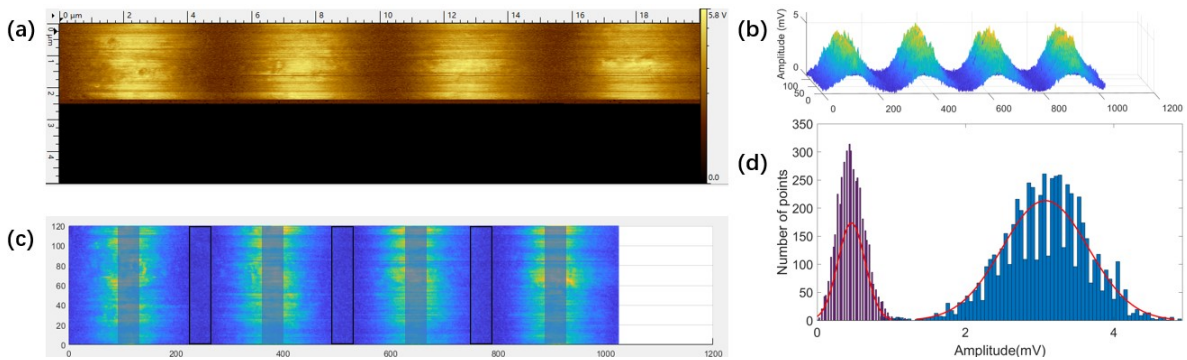


Figure 6.2: (a) Imaged SAW field with excitation frequency in 381 MHz , input power with 12 dbm . (b) Axonometric view of the SAW field imaged by Matlab. (c) Top view of the SAW field imaged by Matlab, the shaded area is the peak part of the SAW field and the black border area is the valley part of the SAW field. (d) The height difference between the peak and valley areas of the SAW field.

SAW field with different frequency Firstly, we imaged the SAW field with different excitation frequencies from 375 MHz to 381 MHz with a frequency gap of 0.5 MHz , the modulated frequency is 20 kHz , and the power is 11 dBm , the relationship between them is shown as Figure 6.3(a). We found that the amplitude of the SAW will change with the change in the activated frequency of the SAW device, which is very similar to the peak part in the S_{21} parameter. Then we attempted to overlap curves simulated S_{21} parameter of the SAW device and amplitude of the SAW vs frequency, as shown in Figure 6.3(b). In this figure, we fitted the simulated S_{21} curve with the measured S_{21} curve and found that the variation trends of these two curves with frequency were consistent. Then we attempted to overlap curves measured S_{21} parameter of the SAW device and amplitude of the SAW vs frequency as shown in Figure 6.3(c). We found that the amplitude of the SAW will change with the activated frequency of the SAW device and the variation trend of amplitude with frequency is the same as that of S_{21} .

parameter.

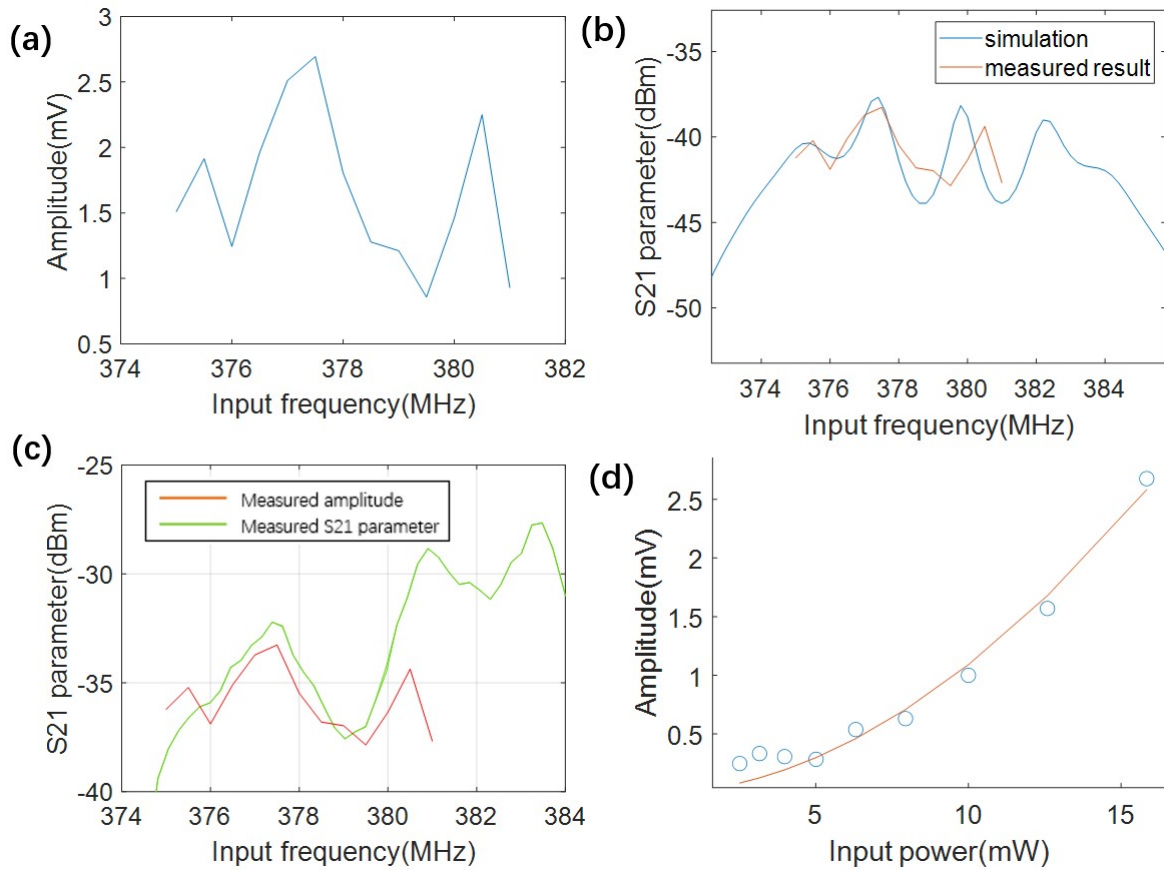


Figure 6.3: (a) Relationship between the amplitude of the SAW field and different input frequencies of the SAW device. (b) Superposition curve of simulated S_{21} parameters of the SAW devices (blue) and the relationship between amplitude and frequency of the SAW device (red). (c) Superposition curve of measured S_{21} parameters of the SAW devices (green) and the relationship between amplitude and frequency of the SAW device (red). (d) Relationship between the amplitude of the SAW field and different input powers.

SAW field with different input We imaged the SAW field with different excitation power from 4 dBm to 12 dBm with 1 dBm intervals, the modulated frequency is 20 kHz, and the input frequency is 381 MHz. Decibel-milliwatts (dBm) is a unit to represent absolute power, the formula for converting power $P(mW)$ to $x(dBm)$ is as follows:

$$x = 10 \log_{10} \left(\frac{P}{1mW} \right) \quad (6.1)$$

and

$$P = (10mW) 10^{\left(\frac{x}{10}\right)} \quad (6.2)$$

The relationship between the input power and the amplitude is shown in Figure 6.3(d), the blue dot represents the amplitude corresponding to the input power we measured, while the red line represents the curve we fitted based on the measured dots. In this figure, We found that the relationship between the amplitude of the SAW field and different input powers is quadratic.

6.3. Imaging the SAW field on the substrate with microcavities

After imaging the SAW field on the SAW device substrate, we fabricate a microcavity on the SAW device, the position and the size of the microcavity are shown in Figure 6.4. The diameter

of the microcavity is $8.78 \mu\text{m}$ and the depth is $0.4 \mu\text{m}$, the horizontal distance between the microcavity to the activated IDTs is $236 \mu\text{m}$ and the vertical distance to the bottom of activated IDTs is $52 \mu\text{m}$.

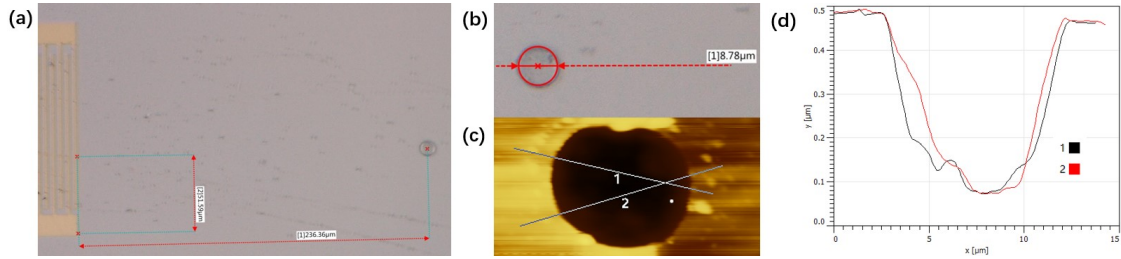


Figure 6.4: (a) Position of microcavity on the substrate. (b) Size of microcavity on the substrate. (c) and (d) Topography of microcavity measured by AFM.

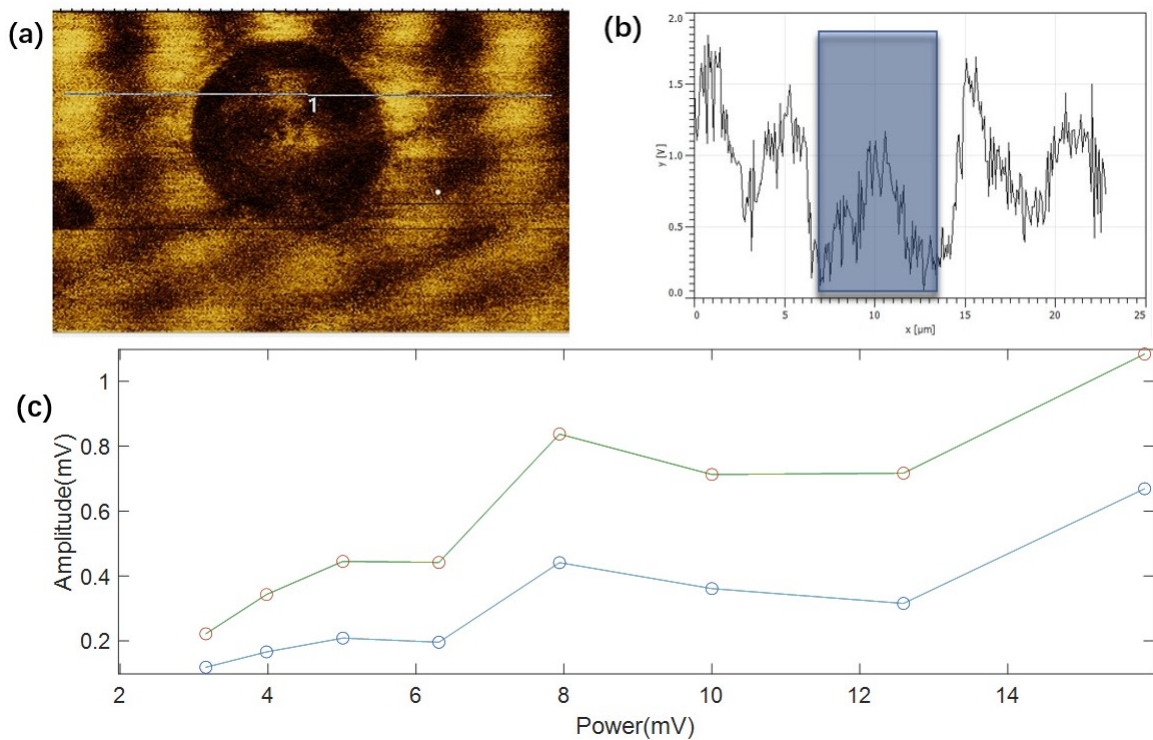


Figure 6.5: (a) SAW field on the substrate and cavities with 381 MHz and 11 dBm input. (b) Topography of the SAW field with 381 MHz and 11 dBm input. (c) The amplitude of the SAW field propagated on the substrate and the microcavities.

Amplitude of the SAW field on substrate and cavities After the fabrication of the SAW field, we use AFM to image the SAW field around the microcavity area with different excitation power from 4 dBm to 11 dBm with the power gap of 1 dBm in 381 MHz , as shown in Figure 6.5. We use Gwyddion to analyse the topography of the SAW field as shown in Figure 6.5(b), the shadow area is the amplitude information of the SAW propagated in microcavity and the other is the height information of the SAW propagated on the substrate, we found that the amplitude of the SAW field in microcavities (shadow area) is smaller than that on the substrate (remaining area). Then we analyse the amplitude information of the SAW field on the substrate and microcavities in the chosen area, which with a width of $1 \mu\text{m}$, a length of $25 \mu\text{m}$,

and the centre point of this area is the centre of the microcavities, the calculation method for amplitude is shown in section 6.2. After that, we tried different input power of the SAW device and analysed the amplitude information of the SAW field on the substrate and microcavities with different input power, the result is shown in Figure 6.5(c). We found that the amplitude of the SAW propagated in microcavities is 53.4% of that propagated on the SAW device substrate, and the trend of amplitude variation is also the same for both, as shown in Figure 6.5(c).

6.4. Imaging the SAW field on the suspended membrane

After the characterisation of the SAW field on the microcavities area, we placed the SAW device in a beaker containing acetone and used Branson 1800 ultrasonic cleaner to clean the device for 10 minutes at the lowest power level. Then, we placed it in a beaker containing IPA and repeated the previous operation. After cleaning the SAW device, we transferred the 2D membrane to fabricated cavities to fabricate the suspended membrane. The fabricated 2D suspended membrane is shown as Figure 6.6(b) and (c).

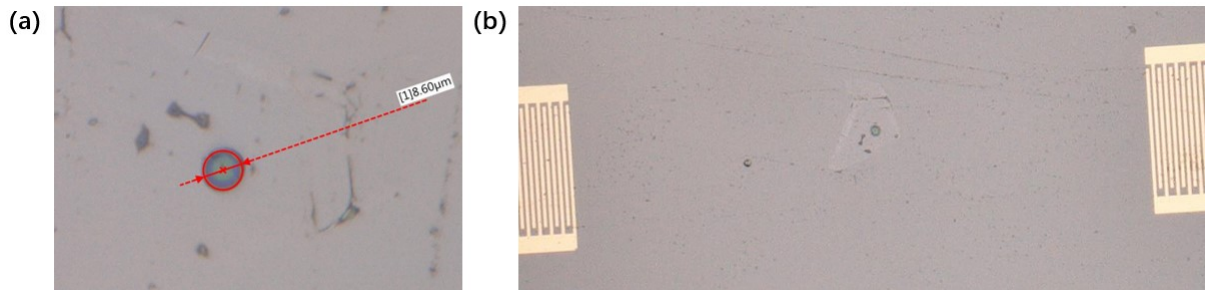


Figure 6.6: (a) Size and shape of the suspended membrane fabricated on the SAW device. (b) Position of the suspended membrane on the SAW device.

6.4.1. SAW Field on Suspended Graphene Membrane

After the suspended membrane fabrication, we measured the SAW field on the suspended graphene membrane. When we use AFM to measure the suspended membrane, we found a dot-like polymer at the edge of the suspended membrane, and the eigenfrequency of the suspended membrane near the polymer will be affected by the polymer, which will affect the propagation of SAW on the suspension membrane. In the SAW field imaging process, we used the signal generator to generate the RF signal with 12 dBm power in 381 MHz, 380.5 MHz and 379 MHz to activate the SAW device. The image of these SAW fields is shown in Figure 6.7.

To find the propagation direction of the SAW field, we used Matlab to analyse the SAW field, the process steps are shown as follows:

- Load the AFM image data into MATLAB and identify the region of interest (ROI) containing the SAW field on the suspended membrane, as shown in Figure 6.8(a).
- Compute the gradient of the wave field in the ROI. We used the gradient function to find the rate of change of the wave field in both the x and y directions and calculated the magnitude and direction of the gradient at each point, as shown in Figure 6.8(b).
- Visualise and analyse the resulting magnitude and direction of the gradient, count the propagation direction of each point and find the propagation direction of the SAW field, as shown in Figure 6.8(c).

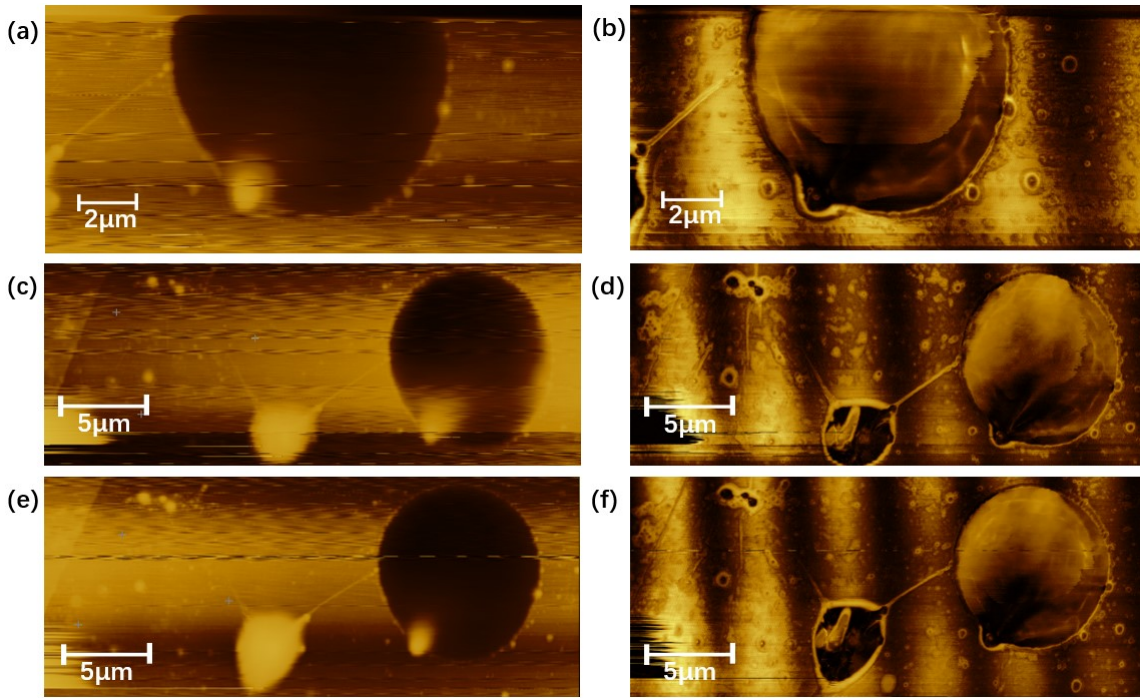


Figure 6.7: (a) Topography of the measured SAW device area in 379 MHz. (b) Imaged SAW field in 379 MHz. (c) Topography of the measured SAW device area in 380.5 MHz. (d) Imaged SAW field in 380.5 MHz. (e) Topography of the measured SAW device area in 381 MHz. (f) Imaged SAW field in 381 MHz.

Propagation Direction In these three sets of images of the SAW field, we found that when the SAW transferred from the supported graphene membrane to the suspended graphene membrane, the propagation direction changed from $+3.2^\circ$ to -11.9° at 379 MHz, from $+3.2^\circ$ to -10.3° at 380.5 MHz, from $+1.5^\circ$ to -9.7° at 381 MHz. + represents upward propagation and – represents downward propagation. The propagation direction of the measured SAW field on the suspended membrane and $LiNbO_3$ substrate at different frequencies are shown in Figure 6.9.

When SAW propagates on the graphene membrane on the $LiNbO_3$ substrate, the SAW field on the graphene membrane on the substrate is the same as that on the $LiNbO_3$. When SAW propagates from $LiNbO_3$ substrate to the suspended membrane, the propagation direction will change due to Snell's law.

Amplitude Variation along the SAW Propagation Direction on Suspended Membrane

After we imaged the SAW field on the suspended membrane at three different frequencies, we measured the vibration amplitude of each point along the SAW propagation direction, as shown in Figure 6.10. The measured wavelength of the SAW propagated on the suspended membrane is $5.6 \mu m$, and the amplitude of the SAW field with different frequencies is consistent with the previous measurements of the SAW propagated on $LiNbO_3$ substrate. As shown in this figure, the amplitude of the SAW propagated on the suspended membrane will decay as the propagation distance increases, the amplitude of the first peak is $2.544 mV$, and the amplitude of the second peak is $0.892 mV$ the attenuation of the amplitude is 64.9%. Due to the size of the suspended membrane, we can not measure the amplitude of the third peak.

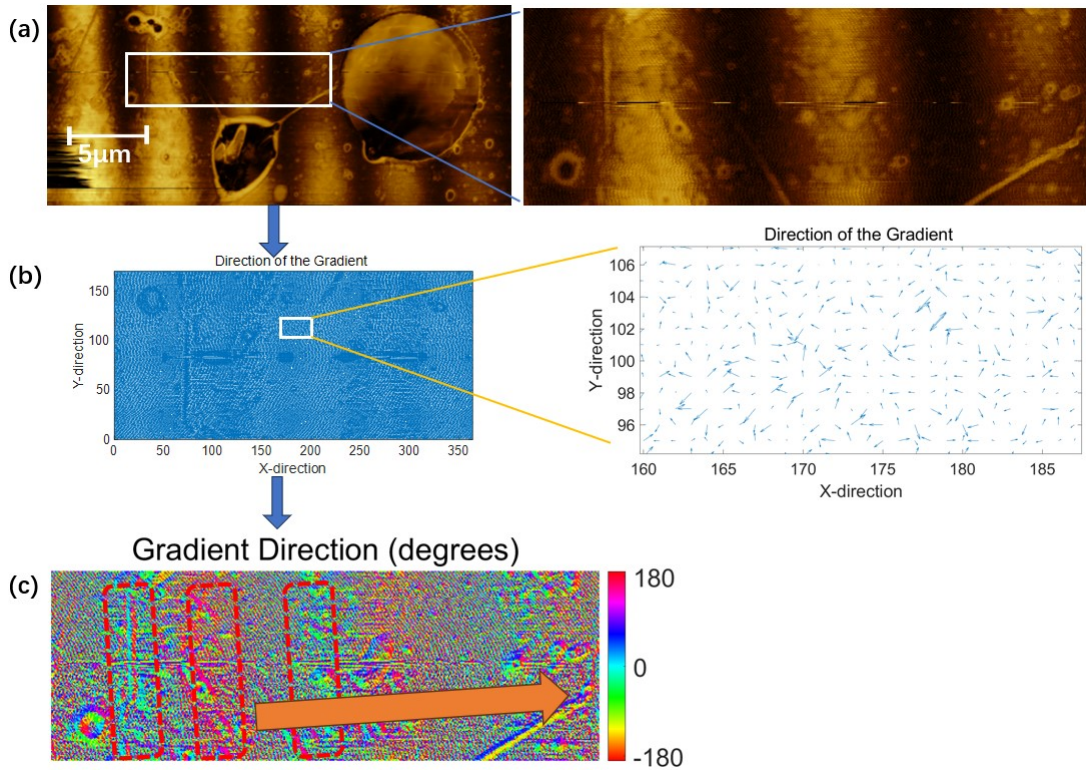


Figure 6.8: (a) Topography of the measured SAW device area in 379 MHz. (b) Imaged SAW field in 379 MHz. (c) Topography of the measured SAW device area in 380.5 MHz. (d) Imaged SAW field in 380.5 MHz. (e) Topography of the measured SAW device area in 381 MHz. (f) Imaged SAW field in 381 MHz.

6.4.2. SAW Field on Graphene Membrane and $LiNbO_3$ Substrate

After imaging the SAW field on the suspended membrane, we characterised the amplitude of the SAW field on the graphene membrane and $LiNbO_3$ substrate, the image of the SAW field is shown as Figure 6.11. In Figure 6.11(a) and (b), we found that the thickness of the fabricated graphene membrane is 6 nm. In Figure 6.11(c), the left part is the SAW field on the membrane, and the right part is the SAW field on the substrate. The amplitude of the SAW field is shown in Figure 6.11(d), we found the amplitude of the SAW field on the graphene membrane is 0.96 mV and the amplitude of the SAW field on the $LiNbO_3$ substrate is 0.64 mV, which means that the amplitude of the SAW field on the graphene membrane is larger than that on $LiNbO_3$ substrate. To explore the amplitude change of the SAW field in different propagation materials, we measure the amplitude of the SAW field in 2 areas, the graphene membrane and the $LiNbO_3$ substrate. The vertical distance of these two regions on the SAW device is 30 μm, and the horizontal distance is 0 μm; both areas are in the centre of the excited SAW field, as shown in Figure 6.12(a). By using the amplitude calculation method mentioned in Section 6.2, we measured the amplitude of the SAW field propagated on graphene membrane and $LiNbO_3$ substrate with 12 dBm input in different frequencies, as shown in Figure 6.12(b). Calculating the average by dividing the amplitudes of the SAW fields propagated in different materials at different frequencies, we found that the average amplitude of the SAW field propagated on $LiNbO_3$ substrate is 0.56 times that on graphene membrane.

We found that this situation is caused by the reason as follow

- **Forced Vibrations:** When the $LiNbO_3$ substrate vibrates, it exerts periodic forces on the graphene membrane. If these external forces' frequency matches the graphene membrane's natural frequency, it experiences resonance. The amplitude of forced vibrations can be larger than the amplitude of the $LiNbO_3$ substrate vibrations alone, leading to a greater displace-

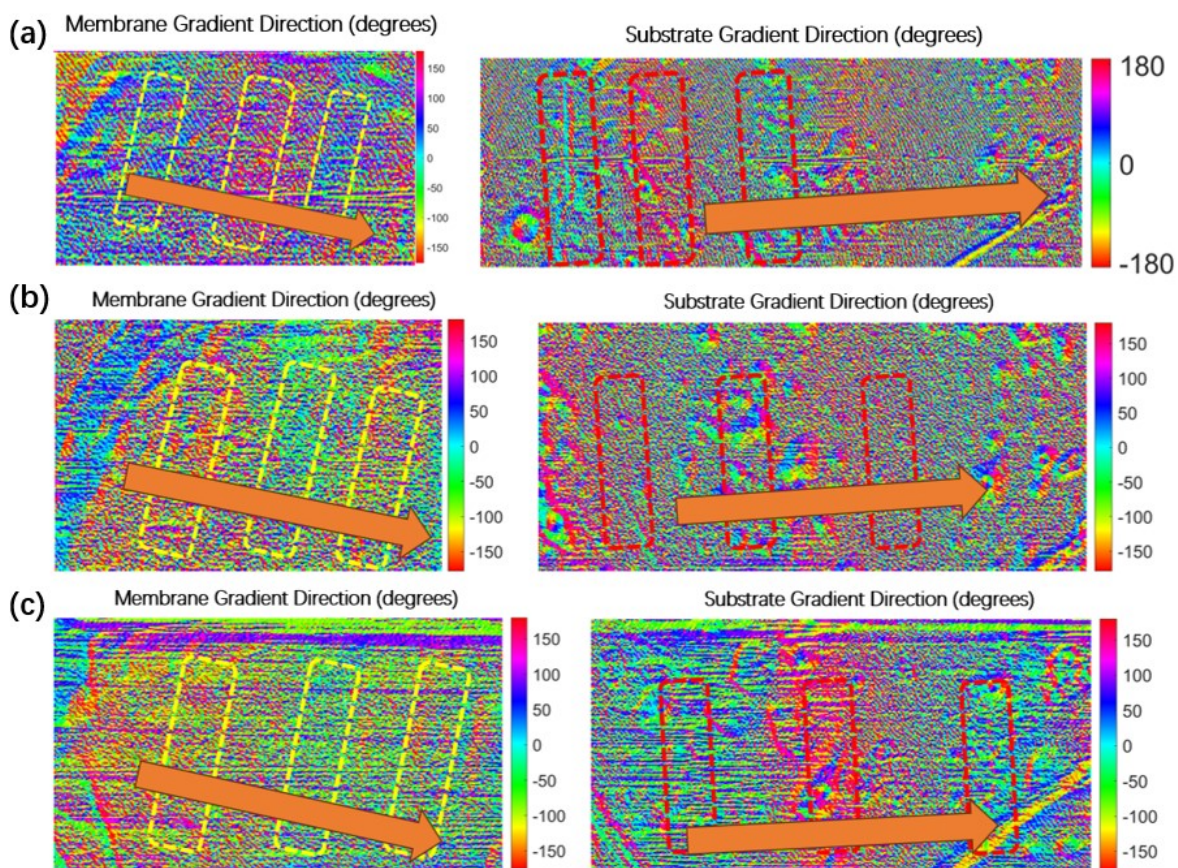


Figure 6.9: (a) Gradient field on the suspended membrane and the $LiNbO_3$ substrate at 379 MHz. (b) Gradient field on the suspended membrane and the $LiNbO_3$ substrate at 380.5 MHz. (c) Gradient field on the suspended membrane and the $LiNbO_3$ substrate at 381 MHz.

ment of the graphene membrane.

Overall, the combination of forced vibrations and damping effects can result in a greater amplitude of the graphene membrane when placed on the vibrating $LiNbO_3$ substrate.

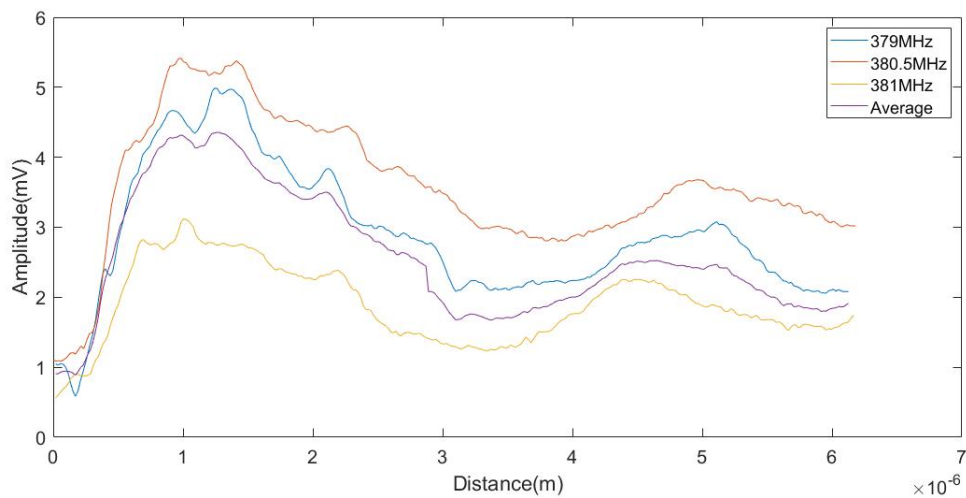


Figure 6.10: Amplitude variation along the SAW propagation direction on the suspended membrane.

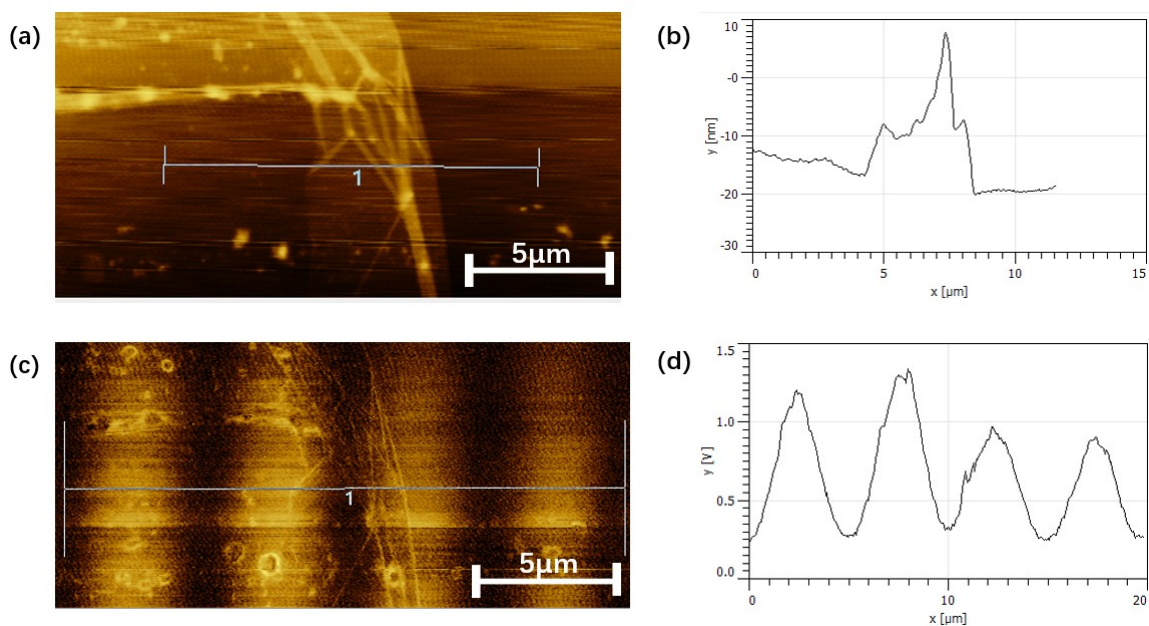


Figure 6.11: (a) Image of the SAW device with graphene and without graphene membranes on the substrate. (b) The surface height variation along the lines marked in Figure (a). (c) Image of the SAW field propagated on graphene membrane and $LiNbO_3$ substrate. (d) The variation of SAW field amplitude along the lines marked in Figure (c).

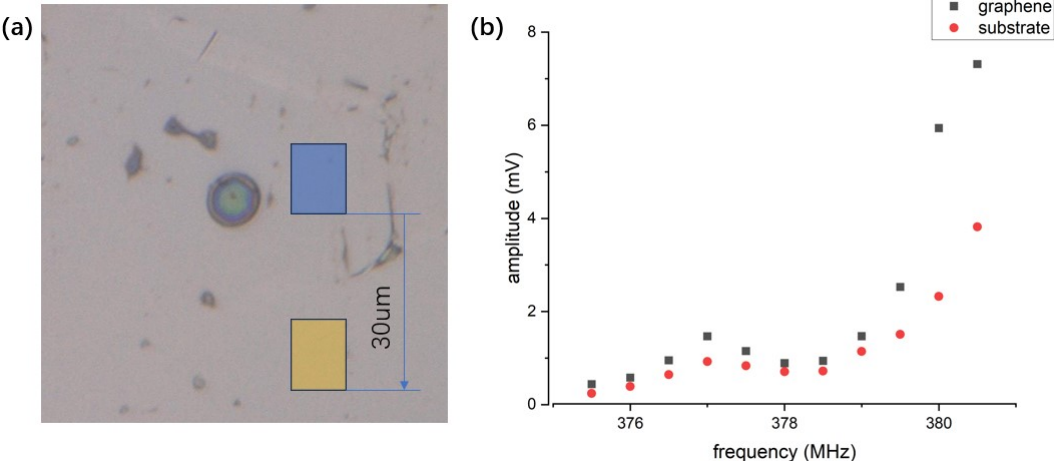


Figure 6.12: (a) Measurement area of the SAW field amplitude, blue is the area of graphene membrane and yellow is the area of $LiNbO_3$ substrate. (b) The amplitude of the SAW field on different propagation materials with 12 dBm input.

7

Conclusion and Outlook

Conclusion

In this project, we focused on imaging the SAW field on the suspended membrane, which can be useful for improving the accuracy of SAW sensors and observing the movement of biomolecules on biomembranes based on SAW operations. To achieve the SAW field imaging, we proposed two imaging methods and attempted them. In Chapter 3, we conducted 2D simulations of the SAW devices to investigate the influence of microcavities parameters on the SAW devices. In Chapter 4, we fabricated microcavities based on the simulation results in Chapter 3 and realized the preparation of the suspended membrane by covering microcavities with a layer of graphene film. In Chapter 5, we attempted to use DHM to image the SAW field but did not achieve the imaging of the SAW fields. In Chapter 6, we successfully imaged the SAW field using AFM and recorded the SAW field with different frequencies and powers.

When measuring the amplitude of the SAW field, we found that the variation trend of amplitude with frequency is the same as that of the S_{21} parameter. When SAW propagates in an area with microcavities, the amplitude of the SAW field in microcavities is smaller than that in the substrate due to the influence of transmission efficiency and irregular morphology at the bottom of the microcavities. Due to the influence of microcavities morphology, at the same phase of the SAW field, the amplitude in the centre area of the microcavities is greater than that in the edge area. When measuring the SAW field on the suspended membrane, we found that the propagation direction of the SAW will change when propagates through the graphene membrane to the suspended membrane due to the initial phase difference of the suspended membrane and the wavelength difference between the graphene membrane and suspended membrane. When exploring the amplitude variation on the graphene membrane, we found that the amplitude of the SAW field will attenuate along the propagation direction on the suspended membrane, and the amplitude of the SAW field will change with the vertical distance from the centre of the suspended membrane. When exploring the propagation of SAW from the $LiNbO_3$ substrate to the graphene membrane, we found that the amplitude of SAW on the graphene membrane is about twice that on the $LiNbO_3$ substrate, which we think is caused by forced vibrations and damping effects.

Once the graphene membrane is transferred to the fabricated microcavities on the SAW device, we begin to image the SAW field to study the propagation of SAW propagated in 2D material. The purpose of these experiments is to answer the research questions raised in Chapter 1. Each of these questions and the relevant conclusions of the experimental results are shown below:

- **How do we image the SAW field?**

In this project, we used two methods to image the SAW field, DHM and SAMF. However, during the process of the SAW field imaging with DHM, we did not achieve imaging of the SAW field due to excessive environmental noise and low amplitude of the SAW field. By using SAMF, we successfully recorded the amplitude of the SAW field with different input frequencies and input powers.

•What is the difference between the propagation of the SAW in microcavities and substrates when SAW propagates on the surface with microcavities?

The amplitude of the SAW field will change when propagated from the substrate to microcavities; the amplitude of the SAW propagated in microcavities is 53.4% of that propagated on the SAW device substrate.

•Is the propagation of SAW on the suspended 2D membrane the same as that on the surface, and how does the 2D membrane affect the propagation of SAW?

The propagation direction of the SAW will change when propagated from the graphene membrane to the suspended membrane. When the SAW propagates from the substrate to the suspended membrane, the wavelength of the SAW will change from $10\ \mu\text{m}$ to $5.6\ \mu\text{m}$. The amplitude of the SAW propagated on the suspended membrane will decay as the propagation distance increases, the amplitude of the second period is 0.35 of the first one.

Outlook

The current image of the SAW field propagated in suspended 2D material can help us understand how the SAW propagates on 2D membranes. In the experimental and simulation of the project, we encountered many challenges which limited the quality of our simulation and experimental results. In order to improve the process and experimental results, many aspects can be improved. These areas that can be improved are summarized below.

- Simulation: Due to computer performance limitations, we only conducted 2D simulations. When exploring the impact of microcavities on the SAW devices, we removed a rectangle area on the substrate of the SAW device for 2D simulation, which is equivalent to adding a groove as wide as the device on the SAW device in 3D simulation, and that may cause errors in the simulation. As for the simulation of the SAW propagated on the suspended membrane, we could not carry it out with our computer, and this simulation can be a good reference in the experiment. The 3D simulation can effectively help us choose reasonable parameters and better understand the motion of the SAW on suspended membranes.

- 2D membrane fabrication: In the 2D membrane transfer, there is a polymer with a diameter of $0.5\ \mu\text{m}$ at the edge of the suspended membrane, and it will affect the vibration of the suspended membrane. If there is no polymer near the suspended membrane, the image of the SAW field on the suspended membrane will be better, and we can know how the SAW will propagate on the suspended membrane better.

- Microcavities fabrication: In the suspended membrane fabrication, we fabricated the suspended membranes by covering microcavities with a layer of graphene membrane, so the shape of the microcavities determines the shape of the suspended membrane. In the experiment, we only achieved the fabrication of circular microcavities with a diameter less than $10\ \mu\text{m}$. If other shapes of microcavities with a diameter less than $10\ \mu\text{m}$ can be prepared, it will help us explore the influence of suspended membrane shape on the SAW propagation.

References

- [1] Lord Rayleigh. "On waves propagated along the plane surface of an elastic solid". In: *Proceedings of the London mathematical Society* 1.1 (1885), pp. 4–11.
- [2] Bertrand Coste et al. "Piezo1 and Piezo2 are essential components of distinct mechanically activated cation channels". In: *Science* 330.6000 (2010), pp. 55–60.
- [3] Bertrand Coste et al. "Piezo proteins are pore-forming subunits of mechanically activated channels". In: *Nature* 483.7388 (2012), pp. 176–181.
- [4] Xiaozhu Zhou et al. "Chemically functionalized surface patterning". In: *Small* 7.16 (2011), pp. 2273–2289.
- [5] David G Grier. "A revolution in optical manipulation". In: *nature* 424.6950 (2003), pp. 810–816.
- [6] Zachary R Gagnon. "Cellular dielectrophoresis: Applications to the characterization, manipulation, separation and patterning of cells". In: *Electrophoresis* 32.18 (2011), pp. 2466–2487.
- [7] Hao Jia, Xia Liu, and Philip X-L Feng. "Manipulating and Patterning Micro/Nanoparticles in Liquid Using Multimode Membrane Resonators". In: *2018 IEEE Biomedical Circuits and Systems Conference (BioCAS)*. IEEE. 2018, pp. 1–4.
- [8] Fredrik Schedin et al. "Detection of individual gas molecules adsorbed on graphene". In: *Nature materials* 6.9 (2007), pp. 652–655.
- [9] Tim J Booth et al. "Macroscopic graphene membranes and their extraordinary stiffness". In: *Nano letters* 8.8 (2008), pp. 2442–2446.
- [10] Nikolaos Tombros et al. "Electronic spin transport and spin precession in single graphene layers at room temperature". In: *nature* 448.7153 (2007), pp. 571–574.
- [11] Weipeng Xuan et al. "Fast response and high sensitivity ZnO/glass surface acoustic wave humidity sensors using graphene oxide sensing layer". In: *Scientific reports* 4.1 (2014), pp. 1–9.
- [12] Stefan Cular, Subramanian KRS Sankaranarayanan, and Venkat R Bhethanabotla. "Enhancing effects of microcavities on shear-horizontal surface acoustic wave sensors: A finite element simulation study". In: *Applied Physics Letters* 92.24 (2008), p. 244104.
- [13] Mujibur Rahman and JR Barber. "Exact expressions for the roots of the secular equation for Rayleigh waves". In: (1995).
- [14] Thorsten Hesjedal. "Surface acoustic wave-assisted scanning probe microscopy—a summary". In: *Reports on progress in Physics* 73.1 (2009), p. 016102.
- [15] Richard M White and Fred W Voltmer. "Direct piezoelectric coupling to surface elastic waves". In: *Applied physics letters* 7.12 (1965), pp. 314–316.
- [16] Ludwig Bergmann, Henry Hatfield, et al. "Ultrasonics and their scientific and technical applications". In: (1938).
- [17] Myung K Kim. "Principles and techniques of digital holographic microscopy". In: *SPIE reviews* 1.1 (2010), p. 018005.

- [18] Tatsuki Tahara et al. "Digital holography and its multidimensional imaging applications: a review". In: *Microscopy* 67.2 (2018), pp. 55–67.
- [19] Neal Brock et al. "Dynamic interferometry". In: *Novel Optical Systems Design and Optimization VIII*. Vol. 5875. SPIE. 2005, pp. 101–110.
- [20] Andreas Brunn et al. "High speed 3D surface inspection with digital holography". In: *Eighth International Symposium on Precision Engineering Measurement and Instrumentation*. Vol. 8759. SPIE. 2013, pp. 929–935.
- [21] Amandeep Singh and Renu John. "Elastography measurement for soft material using digital holography". In: *Fourth International Seminar on Photonics, Optics, and Its Applications (ISPhOA 2020)*. Vol. 11789. SPIE. 2021, pp. 9–16.
- [22] Peng Gao and Caojin Yuan. "Resolution enhancement of digital holographic microscopy via synthetic aperture: a review". In: *Light: Advanced Manufacturing* 3.1 (2022), pp. 105–120.
- [23] Hongpeng Qin, Rikang Qin, and Zhuqing Jiang. "Improvement and denoising for dual-wavelength digital holographic microscopy". In: *Holography, Diffractive Optics, and Applications X*. Vol. 11551. SPIE. 2020, pp. 190–196.
- [24] F Dinelli et al. "Measurements of stiff-material compliance on the nanoscale using ultrasonic force microscopy". In: *Physical Review B* 61.20 (2000), p. 13995.
- [25] T Hesjedal, E Chilla, and H-J Fröhlich. "High resolution visualization of acoustic wave fields within surface acoustic wave devices". In: *Applied physics letters* 70.11 (1997), pp. 1372–1374.
- [26] DR Oliver et al. "Heterodyne electrostatic imaging of polarization due to a surface acoustic wave". In: *Applied Physics Letters* 79.22 (2001), pp. 3729–3731.
- [27] Fanghao Li, Dongxian Zhang, and Haijun Zhang. "Study of AFM-based probe for detecting laser induced surface acoustic wave". In: *2011 International Conference on Electrical and Control Engineering*. 2011, pp. 4988–4990. DOI: 10.1109/ICECENG.2011.6057563.
- [28] Jan Hellemann et al. "Determining amplitudes of standing surface acoustic waves via atomic force microscopy". In: *Physical Review Applied* 17.4 (2022), p. 044024.
- [29] Kailiang Zhang et al. "Two dimensional hexagonal boron nitride (2D-hBN): synthesis, properties and applications". In: *Journal of Materials Chemistry C* 5.46 (2017), pp. 11992–12022.
- [30] Kostya S Novoselov et al. "Electric field effect in atomically thin carbon films". In: *science* 306.5696 (2004), pp. 666–669.
- [31] Xuesong Li et al. "Large-area synthesis of high-quality and uniform graphene films on copper foils". In: *science* 324.5932 (2009), pp. 1312–1314.
- [32] Nicholas R Glavin et al. "Synthesis of few-layer, large area hexagonal-boron nitride by pulsed laser deposition". In: *Thin Solid Films* 572 (2014), pp. 245–250.
- [33] Wenshuai Zhu et al. "Graphene-analogue hexagonal BN supported with tungsten-based ionic liquid for oxidative desulfurization of fuels". In: *ACS Sustainable Chemistry & Engineering* 3.1 (2015), pp. 186–194.
- [34] KS Novoselov and AH Castro Neto. "Two-dimensional crystals-based heterostructures: materials with tailored properties". In: *Physica Scripta* 2012.T146 (2012), p. 014006.
- [35] Olga Zaytseva and Günter Neumann. "Carbon nanomaterials: production, impact on plant development, agricultural and environmental applications". In: *Chemical and Biological Technologies in Agriculture* 3.1 (2016), pp. 1–26.

-
- [36] Andres Castellanos-Gomez et al. "Deterministic transfer of two-dimensional materials by all-dry viscoelastic stamping". In: *2D Materials* 1.1 (2014), p. 011002.
- [37] Ji Won Suk et al. "Mechanical measurements of ultra-thin amorphous carbon membranes using scanning atomic force microscopy". In: *Carbon* 50.6 (2012), pp. 2220–2225.